Doctoral Thesis

Ab initio study of spin-phonon dynamics and band topology through the real-time time-dependent density functional theory

Dongbin Shin

Department of Physics

Graduate School of UNIST

2019

Ab initio study of spin-phonon dynamics and band topology through the real-time time-dependent density functional theory

Dongbin Shin

Department of Physics

Graduate School of UNIST

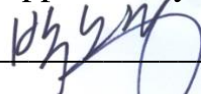# Ab initio study of spin-phonon dynamics and band topology through the real-time time-dependent density functional theory

A thesis/dissertation

submitted to the Graduate School of UNIST

in partial fulfillment of the

requirements for the degree of

Doctor of Philosophy

Dongbin Shin

1. 8. 2019 Month/Day/Year of submission

Approved by

_____

Advisor

Noejung Park

Ab initio study of spin-phonon dynamics and band topology through the real-time time-dependent density functional theory

Dongbin Shin

This certifies that the thesis/dissertation of Dongbin Shin is approved.

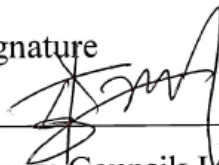1. 8. 2019 Month/Day/Year of submission
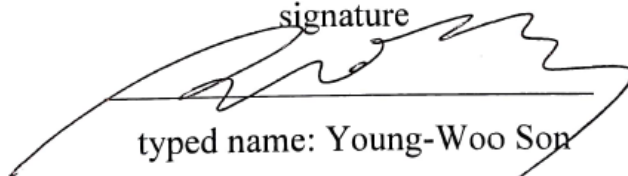
signature

Advisor: Noejung Park

signature

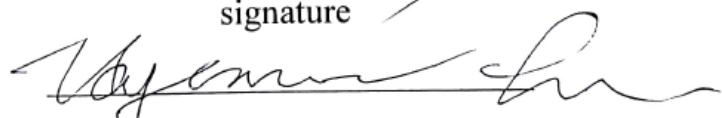typed name: Hosub Jin

signature

typed name: Geunsik Lee

signature

typed name: Young-Woo Son

signature

typed name: Hyun-Woo Lee

Abstract

Among diverse hierarchical theoretical methods in the field of condensed matter, Kohn and Sham's prescription of density functional theory (named the Kohn-Sham equation) is particularly advantageous because of its practicality and simplicity. This equation allows the investigation of the electronic structure of materials on a first-principle basis without requiring inputs derived from prior knowledge. This thesis presents the integration of the Kohn-Sham density-functional equation into a time-evolution package to construct a real-time and time-dependent density functional calculation method. Using this computational tool, the real-time dynamics of electrons in materials were investigated. Numerical analysis of physical phenomena was performed that cannot readily be assessed using simple model-based theories or static calculations. In this thesis, three separate studies are presented. The first is regarding the correlation between the spin state of conduction valley and specific phonon mode in monolayer MoS_2. The second study is the revelation of Berry curvature and band topology in time-propagating Bloch states under static E-field. The last study is on the real-time dynamics of ultrafast charge transfer. The focus is on exhibiting the unique advantages of the real-time propagation calculation method. It is proposed that the real-time propagation package can be further developed as a general tool to be applied to the calculations of material responses upon an infinitesimal probing perturbation or a strong external driver.

Content

Abstract

List of Figures

List of Tables

List of Figures

List of Tables

Ⅰ. Introduction

Since Newton published the equation of motion for a classical point particle, mathematical formulations of physical laws have been pursued toward an ultimately generalized theory. Dynamical laws of physics written in simple mathematical form have allowed versatile predictions of nature, and thus provided a solid foundation for various areas of technological development. At critical moments, observed experimental results have deviated from or even sharply contradicted the contemporary theory. These contradictions have stimulated the development of physical knowledge and enabled the discovery of new properties of nature. In the early 20th century, the distinction between predictions of classical dynamics and experimental observations resulted in the formulation of quantum physics [1]. The unexpected behavior of nature showed brand-new physics phenomena in the quantum world such as wave-particle duality and the indistinguishable property of the particle. Based on these properties, Schrodinger, Heisenberg, and many other pioneers formulated the equation for the quantum mechanics of particles in the microscopic world. Note, it remains difficult to solve for many-body systems with an exact description of the indistinguishable property of quantum particles.

To predict the behavior of quantum particles using the Schrodinger equation, various approaches have been proposed and tested. Among these approaches, Kohn and Sham suggested that the indistinguishable property for a non-interacting particle can be approximated as a local density functional potential [2]. This effective potential makes it possible to describe the effect of a many electron system through the one-body equations, which is called Kohn-Sham equation. Based on this density functional theory (DFT) approach, steady-state properties of materials have been computationally investigated such as geometrical structure, electronic band structure, and magnetism. To explore the real time dynamics of electronic structure beyond the steady-state, the time propagation of the electron wavefunction in material has also been investigated using the time-dependent DFT (TDDFT) method and the time-profile of observable quantities evaluated by time-propagating wavefunctions, which can be directly compared with experimental observation [3, 4].

In this thesis, DFT and TDDFT are briefly reviewed. Intriguing physical phenomena related to real time dynamics are then introduced. In particular, three different studies in materials are presented as examples of real time dynamics. The first study is on spin-phonon interaction and phonon induced magnetism in monolayer MoS_2 [5]. In this study, it is found that the spin expectation value of conduction band valley state in monolayer MoS_2 shows large variation according to the specific phonon mode. Based on this spin-phonon interaction, phonon-induced spin-Floquet magnetism is suggested. The second topic is revelation of material Berry curvature and band topology in the time-propagating Bloch state [6]. The non-zero Berry curvature in the Brillouin zone generates the anomalous velocity of the Bloch state under the static E-field. Through the evaluation of the expectation value of the velocity

operator around the Brillouin zone under a static E-field, the quantum anomalous Hall conductivity and quantum spin Hall conductivity in 2D topological materials were obtained. The last study is a real-time dynamics simulation of ultrafast charge transfer [7]. Through an Ehrenfest dynamics simulation, the non-equilibrium dynamics phenomena of ultrafast charge transfer are evaluated depending on the initial kinetic energy of the ionic system. These three studies reveal the advantages of the real-time dynamics method that cannot be understood by steady state electronic structure. It was found that the time-profile of the physical observable becomes an important indicator to understand real time dynamics in materials. The real time dynamics calculated using the TDDFT method are used to investigate time propagating electron states under external perturbations.

Ⅱ. Theoretical background and computational details

2.1. Density functional theory

2.1.1. Kohn-Sham equation

In 1960, Hohenberg and Kohn published two important theorems for the calculation of a system of non-interacting particles [8]. The first theorem proves that the electron density is determined by the external potential. The second theorem reveals that the ground state energy can be obtained from the variational principle. Based on these two theorems, the effective one-body equation (called the Kohn-Sham equation) was introduced to evaluate the ground states of many electron systems. In this equation, the local density functional is employed to describe the electron-electron exchange and correlation interactions. By solving the Kohn Sham equation, the ground electron wavefunction and quasiparticle energy level can be evaluated. The Kohn Sham equation can be written as follows

$$\left[-\frac{1}{2}\nabla^2 + V_{ion}(\vec{r}) + V_{Columb}\left[\rho(\vec{r})\right] + V_{XC}\left[\rho(\vec{r})\right] \right]\psi(\vec{r}) = \varepsilon\psi(\vec{r}) \quad (2.1),$$

where V_{ext}, V_H, and V_{ex} are the electron-ion coulomb potential, electron-electron coulomb potential, and electron-electron exchange-correlation potential, respectively.

In the early stages of DFT development, Kohn and Sham suggested electron-electron exchange interactions between non-interacting electrons in material can be approximated as the exchange interaction of homogenous electron gas.

$$V_{XC}^{electron-gas}\left[\rho(\vec{r})\right] = 3\pi/4\rho(\vec{r}) \quad (2.2)$$

Although the many-body interactions between identical electrons cannot be solved exactly, this simple assumption makes it possible to describe the electronic structure of real material. After this suggestion, the more precise exchange functional has been investigated for the accurate description of electronic structure. The local density approximation (LDA) contains an exchange interaction term of homogenous electron gas and additional correlation term to compensate for the missing parts compared with the many-body interaction [9]. In addition, the spin state of an electron in the system is considered by assigning two distinguishable spin states. As a result, the steady state properties of a material (such as lattice parameter and band gap) may be calculated under the DFT scheme.

For an improved description of material properties using the *ab initio* approach, a generalized gradient approximation method is proposed which adds the gradient of the charge density term on the LDA functional [10]. However, there are still problems in describing material properties related to many body interactions of electrons by solving the one-body equation. For example, the band gap calculated by DFT often fails to match the experimentally measured optical band gap. This difference comes from the many body effect of photo excitation. To evaluate the many-body interaction of excited carriers from the ground state electronic structure, Hedin suggested the self-consistent equation called Hedin's

cycle [11]. Based on his study, the optical band gap could be evaluated by DFT calculation with a correction for the many body interaction. For example, the GW approximation deals the two bodies interaction between hole and negative charge screening, and electron and positive charge screening and Bethe-Salpeter equation includes the four bodies interaction between hole, electron, negative and positive charge screening. There are similar approaches to evaluate the other many body effects under the DFT calculation such as the DFT+DMFT method [12].

2.1.2. Self-consistent field and basis set

Currently, computational packages for DFT calculation are mainly developed by a few professional groups. These packages have their own merits related to numerical calculation and technique. The computational algorithms used can be categorized depending on the basis set type for the electron wavefunction description. For example, the plane wave basis set is specialized to describe 3D periodic systems and is employed in the VASP, Quantum ESPRESSO, and Abinit packages [13-15]. However, the computational code with plane wave basis set incurs high computational cost for the Fourier transform process. The numerical grid basis set (employed in the Octopus package) can describe the various dimensional periodic system. The localized atomic orbital basis set (employed in the Siesta package) incurs low computational costs by use of an additional numeric algorithm. The full-potential linearized augmented plane wave basis set (employed in the Wien2k and ELK packages) can deal with the all electron structure using augmented core wavefunctions. While each basis set has particular computational issues associated with implementation, the main algorithm of the DFT calculation is generalized.

The DFT self-consistent loop with plane wave basis set is shown in Figure 2-1. At the initial stage of the DFT calculation, the KS Hamiltonian of the system should be set. Atomic geometry, initial charge density, and basis set for KS states are required to construct the initial KS Hamiltonian. To construct the initial charge density ($\rho^{init}(\vec{r}) = \sum_{n}^{occ} \left| \psi_n^{guess}(\vec{r}) \right|^2$), guessed atomic orbital states ($\psi_n^{guess}(\vec{r})$) are used.

After the construction of the KS Hamiltonian, the KS wavefunction ($\psi_n^{KS}(\vec{r})$) and KS eigenvalues (ε_n^{KS}) are evaluated using diagonalization. The KS wavefunctions obtained are expressed in the given basis set. For example, the KS wavefunction in the plane wave basis set can be described as follows

$$\psi_n^{KS}(\vec{r}) = \sum_{\vec{G}}^{E_{cut}} C_n(\vec{G}) e^{i\vec{G}\cdot\vec{r}}$$, where E_{cut} is maximum kinetic energy of the plane wave. The new charge density ($\rho^{new}(\vec{r}) = \sum_{n}^{occ} \left| \psi_n^{KS}(\vec{r}) \right|^2$) can be constructed using the obtained KS wavefunctions. The non-linearity of the KS equation allows the new Hamiltonian (constructed using the new charge density) to provide a new KS wavefunction that is different from that previously obtained. Therefore, KS equations are self-consistently solved by updating the KS Hamiltonian. If the conserved criteria (such as charge density and total energy difference) are reached, the self-consistent loop is terminated. This process is a general self-consistent field algorithm of the DFT calculation. As a result, the ground state KS wavefunctions and eigenvalues can be obtained.
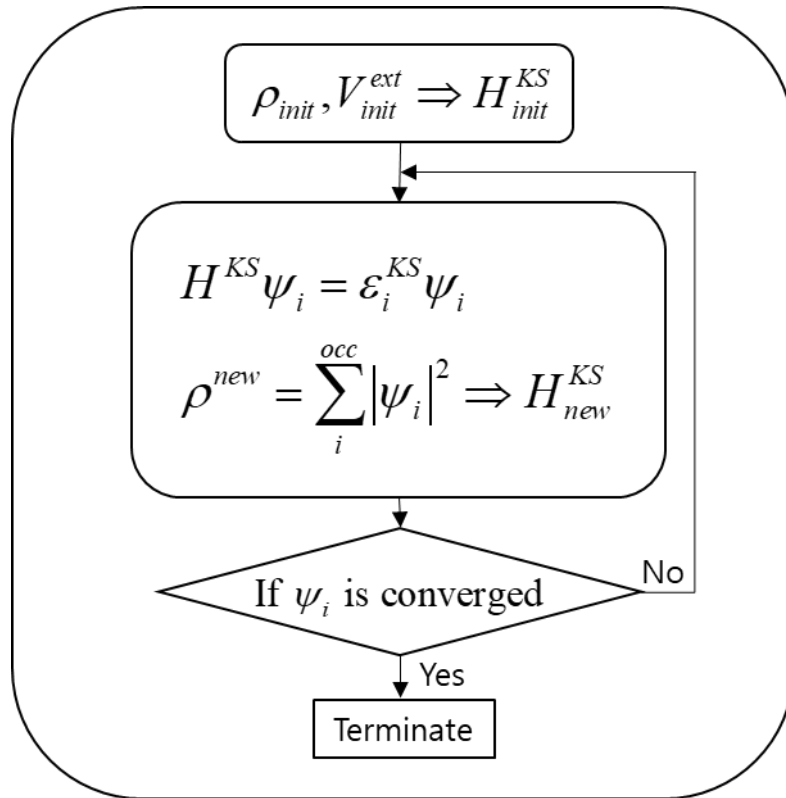
Figure 2-1. Flowchart for DFT self-consistent calculation

2.1.3. Pseudopotential

Effective approximation can significantly reduce computational costs. An example of an effective approximation method in the DFT calculation is the pseudopotential method [16]. This method is based on the simple idea that the core level electrons remain in their atomic orbital states, while valence atomic orbital states are redistributed by external perturbation. Under this assumption, only valence electron states in the KS Hamiltonian are considered. Additional potentials, called pseudopotentials, should be employed to compensate for the interactions between core atomic orbital and valence electron states. To generate the pseudopotential, all electron wavefunctions of a single atom system obtained by DFT calculation are required as follows:

$$\left[-\frac{1}{2}\frac{d^2}{dr^2} + \frac{l(l+1)}{2r^2} - \frac{Z}{r} + \int \frac{\rho(r')}{|r-r'|}dr' + \mu_{xc}[\rho] \right] rR_{nl}^{AE}(r) = \varepsilon rR_{nl}^{AE}(r) \quad \text{. (2-3)}$$

With all electron wavefunctions, pseudo wavefunctions and pseudopotentials can be evaluated. Using the spherical symmetry of a single atom system, only the radial part of the wavefunction can be considered. The pseudo wavefunctions obtained should satisfy several conditions compared with the all electron KS wavefunctions as follows:

$$\left[-\frac{1}{2}\frac{d^2}{dr^2} + \frac{l(l+1)}{2r^2} + V_{l,sc}^{PP}(r) \right] rR_{nl}^{PS}(r) = \varepsilon_l rR_{nl}^{PS}(r),$$

$$V_{l,sc}^{PP}(r) = \varepsilon_l - \frac{l(l+1)}{2r^2} + \frac{1}{2rR_l^{PS}}\frac{d^2}{dr^2}\left[rR_l^{PS}(r) \right]$$

(2-4)

As a result, the pseudopotential for a given total angular momentum is given by:

$$V_l^{PP}(r) = V_{l,sc}^{PP}(r) - \int \frac{\rho_v(r')}{|r-r'|}dr' - \mu_{xc}[\rho_v],$$

$$\rho_v(r) = \sum_{l=0}^{l_{max}} \sum_{m=-l}^{l} \left| rR_l^{PS}(r) \right|^2$$

(2-5)

In the KS Hamiltonian, the pseudopotential in Eq. 2-5 is used instead of the all electron potential.

2.1.4. Hubbard U potential in DFT

Under the DFT scheme, the exchange-correlation potential sometimes fails to describe the charge transfer situation. This problem is called the over-delocalized problem. For example, the DFT calculation provides the negligible band gap of a Mott insulator (such as NiO), while its wide band gap is observed experimentally [17]. To remedy this problem of exchange-correlation functional, DFT with Hubbard U potential (DFT+U) method is employed [7, 17-19]. In this method, occupation dependent non-local potential enhances the on-site Coulomb interaction of the atomic orbital site. This DFT+U energy consists of occupation numbers of atomic orbital sites as follows:

$$E_{Hub} = \frac{U}{2} \sum_{I} \sum_{m,\sigma} \left\{ n_{mm}^{I\sigma} - \sum_{m'} n_{mm}^{I\sigma} n_{m'm}^{I\sigma} \right\},$$

$$\text{while } n_{I\sigma} = \sum_{k} \left\langle \psi_{k\sigma} \left| \hat{P}_I \right| \psi_{k\sigma} \right\rangle f\left(\varepsilon_k\right) \text{ and } P_I = \sum_{m,m'} \left| \phi_m^I \right\rangle \left\langle \phi_{m'}^I \right|.$$

(2-7)

when the projection operators (P_I) are made up of atomic orbital states (ϕ_m^I). The occupation numbers ($n_{I\sigma}$)of atomic orbital states are evaluated by applying the atomic orbital projector to the occupation of KS states ($f\left(\varepsilon_k\right)$). From the Euler-Lagrange equation, the potential for DFT+U is given as follows:

$$\hat{V}^{DFT+U} \left| \psi_{k\sigma} \right\rangle = \hat{V}^{DFT} \left| \psi_{k\sigma} \right\rangle + \sum_{I} U \left(\frac{1}{2} - n_{I\sigma} \right) \hat{P}_I \left| \psi_{k\sigma} \right\rangle . \quad (2\text{-}8)$$

Depending on the occupation number of the atomic orbital state in the KS state, this DFT+U potential provides the negative and positive potential. If a system shows single occupation for the 1s orbital state, the DFT+U potential shifts -0.5U energy for 1s KS orbital state. As a result, it enforces the integer occupation of atomic orbital states (0 or 1 occupations).

2.2. Time dependent density functional theory

2.2.1. Introduction

The ground state electronic structure and related material properties have been studied by solving the KS equation. However, the non-equilibrium dynamics of the electron carrier cannot be described by DFT calculation. In 1984, Runge and Gross introduced an important theorem for time-dependent quantum simulation [20]. The theorem proves the one to one mapping between time-varying electron density and external scalar potentials and is the time-dependent version of the Hohenberg-Kohn theorem. Based on this theorem, time-dependent density functional theory (TDDFT) has been developed [3, 7, 21]. This method has been used to explore optical properties, light-matter interaction, and non-equilibrium dynamics in condensed matter. There are two different approaches in the TDDFT scheme. The first approach is linear response (lr-) TDDFT, which evaluates the optical properties of a material in the frequency domain (such as the dielectric function). The second approach is real time propagation (rtp-) TDDFT, which proceeds the time-evolution of KS states by applying the time-evolution operator. In this thesis, the rtp-TDDFT method is used to investigate the real time dynamics of electron states in materials.

2.2.2. Time-evolution operator in rtp-TDDFT scheme

In the rtp-TDDFT scheme, construction of the time evolution operator (derived from the time-dependent KS equation) is the first step for time-propagation. The operator is written as:

$$U(t+dt,t) = \exp\left(-i\frac{\hat{H}}{\hbar}dt\right) \quad (2\text{-}8)$$

By applying the time-evolution operator on the KS wavefunctions in the previous time step, the wavefunction at next time step is obtained:

$$\psi(t+dt) = U(t+dt,t)\psi(t) \quad (2\text{-}9)$$

In practical computation, there are various forms of time-evolution operator depending on the numerical technique being used. For example, the Suzki-Trotter type split time-evolution operator has an exponential form [4]. The KS Hamiltonian is composed of kinetic, non-local, and local terms which do not commute. To maintain the unitary property of the time-evolution operator with these non-commuting components, the divided exponential operators of kinetic and non-local terms are split by size of local term in the 2nd order Suzki-Trotter type split time-evolution operator as follows:

$$U_{2nd}^{ST}(t+dt,t) = \exp\left(-i\frac{\hat{T}}{2\hbar}dt\right)\exp\left(-i\frac{\hat{V}_{NL}}{2\hbar}dt\right)$$
$$\times\exp\left(-i\frac{V_{Local}}{\hbar}dt\right)\exp\left(-i\frac{\hat{V}_{NL}}{2\hbar}dt\right)\exp\left(-i\frac{\hat{T}}{2\hbar}dt\right) \quad (2\text{-}10)$$

However, this method incurs a high computational cost during application of the exponential type time-evolution operator on the KS wavefunction. Instead of this exact exponential form, the Crank-Nicholson type time-evolution method employs the linear equation solver. As a result, it provides a much more efficient computational algorithm compared with the exact exponential time evolution operator scheme. The Crank-Nicholson type time-evolution operator scheme is based on the time-reversal symmetric propagation between time forward and backward wavefunctions as follows [7]:

$$U\left(t+\frac{dt}{2},t+dt\right)\psi(t+dt) = U\left(t+\frac{dt}{2},t\right)\psi(t) \quad (2\text{-}11)$$

By Taylor expansion of the exponential operator up to first order, the 2nd order Crank-Nicholson type time-evolution operator is obtained:

$$\psi(t+dt) = \frac{1-iHt/2\hbar}{1+iHt/2\hbar}\psi(t) \quad (2\text{-}12)$$

When the Hamiltonian and KS wavefunction at time t is given, in the numerical calculation, Eq. 2-12 becomes the simple linear equation problem:

$$(1+iHt/2\hbar)\psi(t+dt) = (1-iHt/2\hbar)\psi(t) \quad (2\text{-}13)$$

To compare the two different time evolution schemes, benchmark tests were performed with various

systems. To compare the accuracy of the time evolution operators, the numerical error of the total energy ($\delta E(t) = E_{tot}(t) - E_{tot}(0)$) is evaluated during the time-evolution of the steady state KS wavefunctions. The time-propagation of an Al dimer system is evaluated by Crank-Nicholson and Szuki-Trotter type time-evolution operators with various time steps, as shown in Fig. 2-2(a). A smaller time step provides accurate time-propagation, showing less numerical error in the KS total energy in both time-evolution operator calculations. However, there is negligible accuracy difference between the Crank-Nicholson and Szuki-Trotter type time-evolution operators. In Fig. 2-2(b), the computational cost is evaluated with various systems: Al dimer, Benzene molecule, and indolequinone-methide (MQ) molecule. The computational time cost of the Szuki-Trotter type time-evolution operator grows logarithmically with respect to the number of KS states. The computational cost of the Crank-Nicholson type time-evolution operator is comparably small. Hence, the Crank-Nicholson type time-evolution operator is more practical than the Szuki-Trotter type.
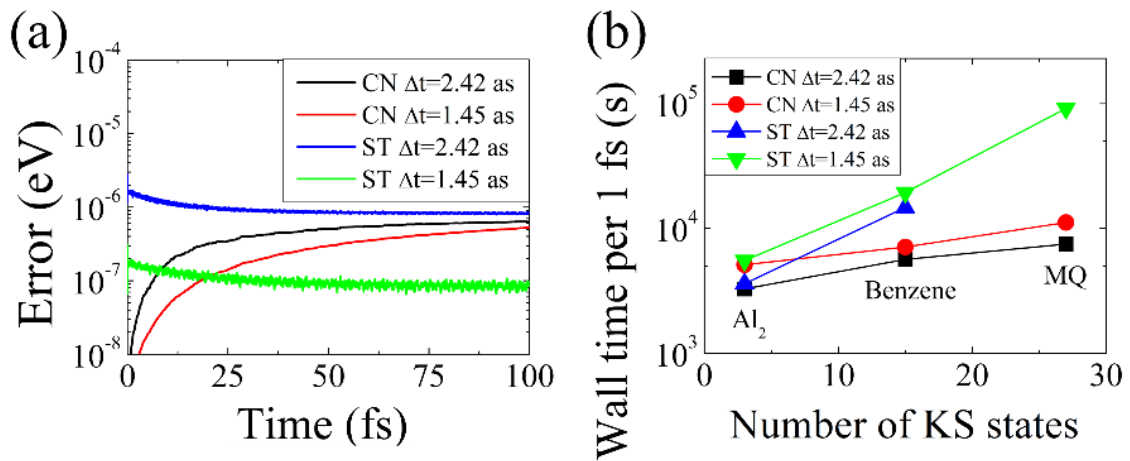
Figure 2-2. (a) Numerical error and (b) computation time cost for TDDFT calculation with various conditions.

2.2.3. Born-Oppenheimer and Ehrenfest dynamics

To evaluate the material system under the DFT scheme, electronic and ionic systems are treated separately. The steady state electron system is evaluated by solving the KS equation [22]. The ionic motion is evaluated by solving the Newtonian equation of motion with the Hellman-Feynman force term. In this approach, the electrons are always following the equilibrium state with the given ionic position. This treatment is based on the Born-Oppenheimer approximation which posits that there is always faster electronic motion enough to reach ground electronic structure comparing with ionic motion by heavier atomic mass. However, TDDFT calculation can treat the non-equilibrium electronic motion by applying the time-evolution operator [7]. As a result, the electronic and ionic motion can be described beyond the Born-Oppenheimer dynamics. By proceeding the electronic and ionic motion with the same time step (called Ehrenfest dynamics), the real time dynamics of interaction between electronic and ionic system can be evaluated

Ⅲ. Phonon-induced valley-Floquet magnetism in monolayer transition metal dichalcogenides

3.1. Transition metal dichalcogenides and vallytronics

The developments of laser technology have enabled to investigate ultrafast optical response of materials. Recent pump and probe experiments show that the valley selective carrier excitation and observation of its valley polarization are demonstrated in monolayer MoS_2 [23, 24]. By the strong spin-orbit coupling (SOC) interaction and absence of inversion symmetry, valence band maximum valleys at K and Kʽ have spin splitting gaps in the monolayer MoS_2 [25]. This electronic structure makes it possible that the circularly polarized light with band gap resonant frequency generates the spin and valley polarized excited carrier in conduction band minimum (CBM) valley at K or K` point depending on the helicity of circularly polarized light as shown in Figure 3-1a. As a result, we can write and read the information in valley states of monolayer MoS_2 through the optical response. To make this phenomenon a useful application, various optical properties in monolayer MoS_2 have been investigated in aspects of excited carrier life time and carrier separation. Some studies revealed that the spin and valley polarized states are rapidly disappeared at high temperature [26]. Especially, the ultrafast spin dynamics of excited carrier is observed at the CBM valley state. In this study, I investigate the physical origin of ultrafast spin depolarization in CBM valley of monolayer MoS_2.
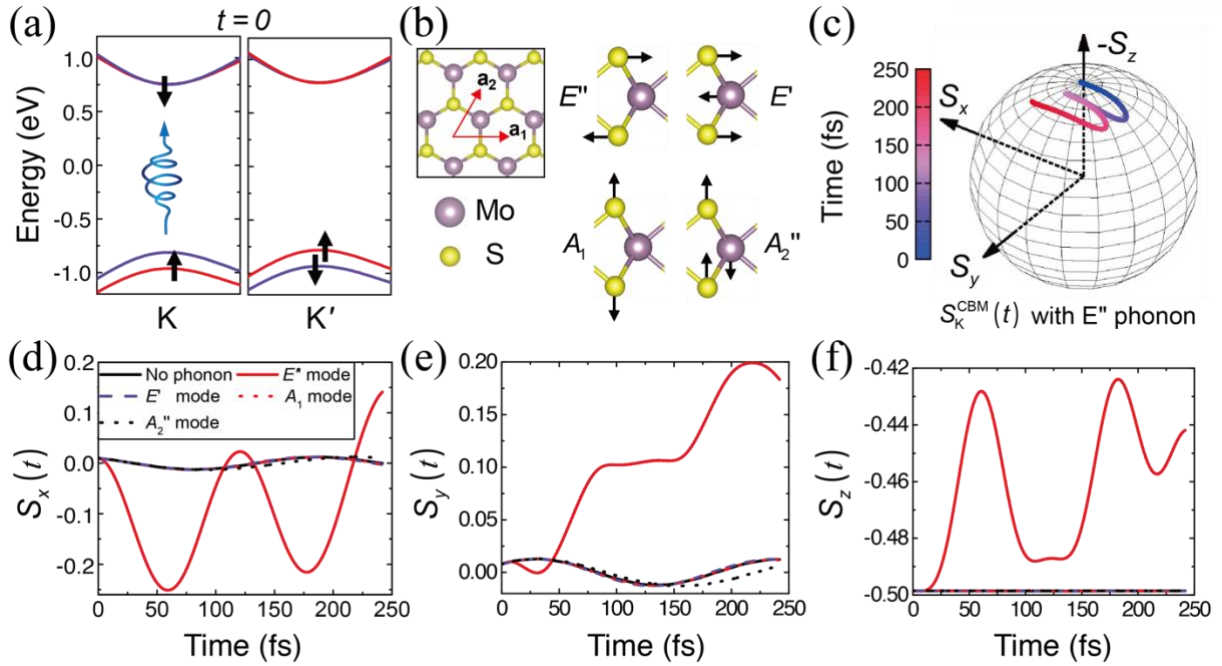
Figure 3-1. (a) The carrier distribution for the spin and valley polarized excitation by circularly polarized light. (b) Top view of monolayer MoS_2 and side views with eigenvectors of optical phonons. (c) Time profile of the spin expectation value of the conduction band maximum valley state under presence of coherent E'' phonon. (d-f) time profiles of spin expectation value with each of coherent phonon modes E'', E', A_1, A_2'' and with the frozen lattice.

3.2. Ultrafast spin dynamics in monolayer MoS$_2$

The geometry of 2H phase of TMDC consist of one transition metal atom and two chalcogenide atoms, and they are inversion asymmetrically distributed in the hexagonal structure as shown in Figure 3-1b(left). As a representative example material, the monolayer MoS$_2$ is employed to investigate the ultrafast spin dynamics of its CBM valley state. Monolayer MoS$_2$ has four optical phonon mode at Γ point as shown in Figure 3-1b(right). The E`` phonon mode shows the alternating in-plane oscillation between two S atoms. The E` phonon mode shows the alternating in-plane oscillation between Mo atom and two S atoms. The A$_1$ phonon mode shows the alternating out-plane oscillation between two S atoms. The A$_2$`` phonon mode shows the alternating out-plane oscillation between Mo atom and two S atoms. With coherent motion of each phonon mode, the spin dynamics of CBM valley state are investigated using TDDFT calculations. For the initial carrier distribution ($t=0$), spin and valley polarized excited carrier at K point is prepared as shown in Figure 3-1a. To investigate effect of coherent phonon mode, the initial atomic velocity is set toward the eigenvector of each phonon mode. When coherent E`` phonon mode is presented in the monolayer MoS$_2$, interestingly, we found that the spin of CBM valley state is dramatically changed within the few hundred femtoseconds comparing with other phonon modes as shown in Figure 3-1c to 3-1f. It is noteworthy that the effect of E`` phonon mainly induces the ultrafast spin dynamics of CBM valley state. In addition, the time scale of spin dynamics consists with previous experimental result which reveals the spin depolarization of CBM valley state within few hundred femtoseconds [26].
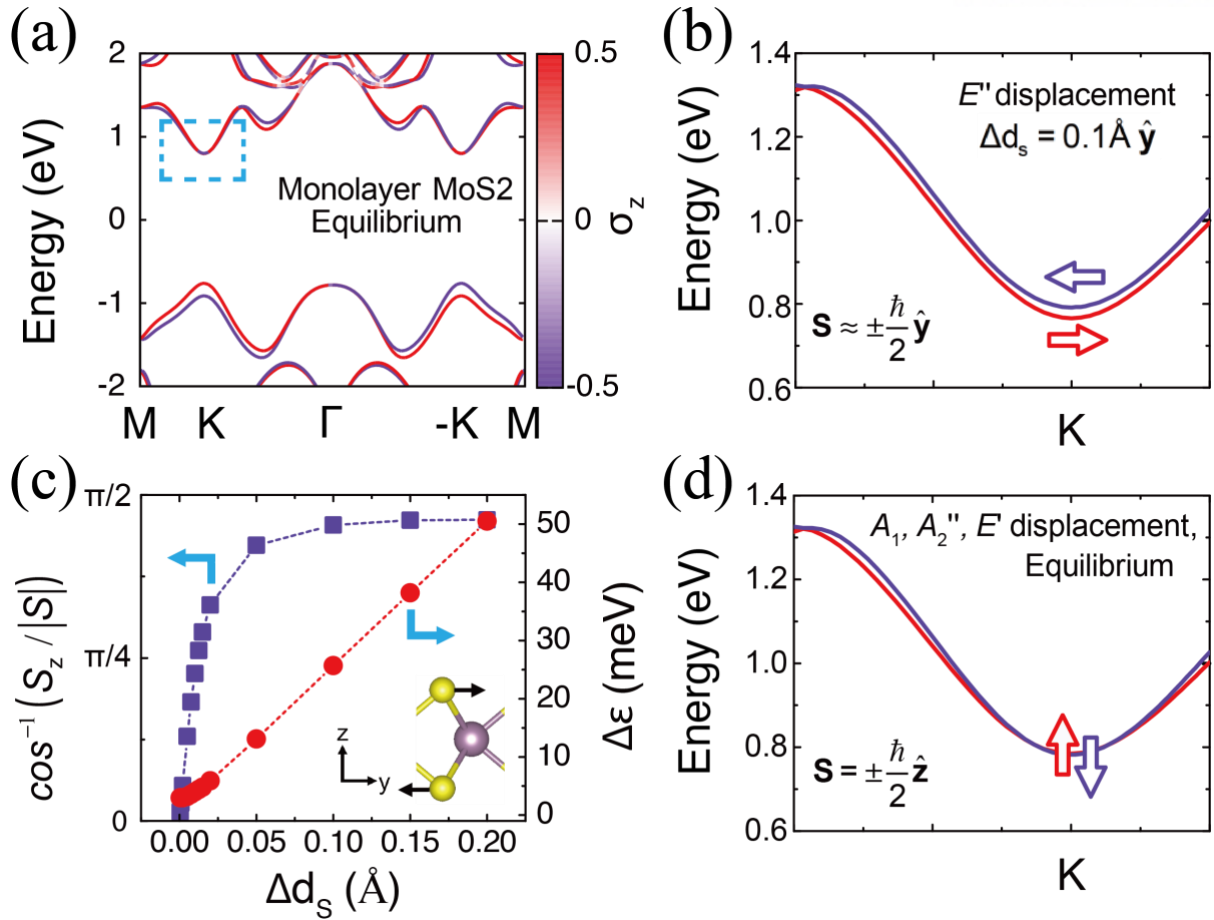
Figure 3-2 (a) Band structure of monolayer MoS_2. (b) Band structure of the conduction band maximum valley with displaced along E'' phonon. (c) The inclination angle and splitting gap ($\Delta\varepsilon_{gap}$) of conduction band valley spin state displaced along E'' phonon. (d) Band structure with the equilibrium geometry and displaced atomic geometry along E', A_1, A_2'' phonon. In (b) and (d), the atomic displacement is scaled with given maximum atomic position shift 0.1Å. The dashed blue box in (a) indicates the area in (b) and (d).

3.3. Effect of E`` phonon mode and effective magnetic field

To understand the detail physics of E`` phonon mode on the spin of CBM valley state, the static electronic structure of monolayer MoS_2 is investigated using DFT calculation. By the spin-orbit coupling interaction and absence of inversion symmetry, Monolayer MoS_2 has large spin splitting gap ($\Delta_{spin}^{VBM} = 156meV$) in valence band maximum (VBM) valley states and comparably small spin splitting gap ($\Delta_{spin}^{CBM} = 3meV$) in CBM valley states at K and K` points, as shown in Figure 3-2a. These spin states of CBM and VBM valleys are both polarized along the out-plane direction. To understand the role of E`` phonon mode on the static CBM valley state, the band structure of monolayer $MoS_2$ with atomic position displaced geometry toward eigen vector of E`` phonon mode is evaluated as shown in Figure 3-2b. This band structure shows changed CBM valley state which has the increased spin splitting gap and the spin polarized states along the in-plane direction, which direction is parallel to atomic position displaced direction. This behavior of CBM valley state with respect to amplitude of atomic displacement is summarized in Figure 3-2c. It shows that the larger atomic displacement along the eigen vector of E`` phonon mode induces the higher spin splitting gap and inclination spin angle of CBM valley states. This result reveals that the atomic displacement along the eigen vector of E`` phonon mode provides effective in-plane magnetic field from the SOC term. On the other hand, there is no significant variation on CBM valley state comparing with E`` case as shown in Figure 3-2d.
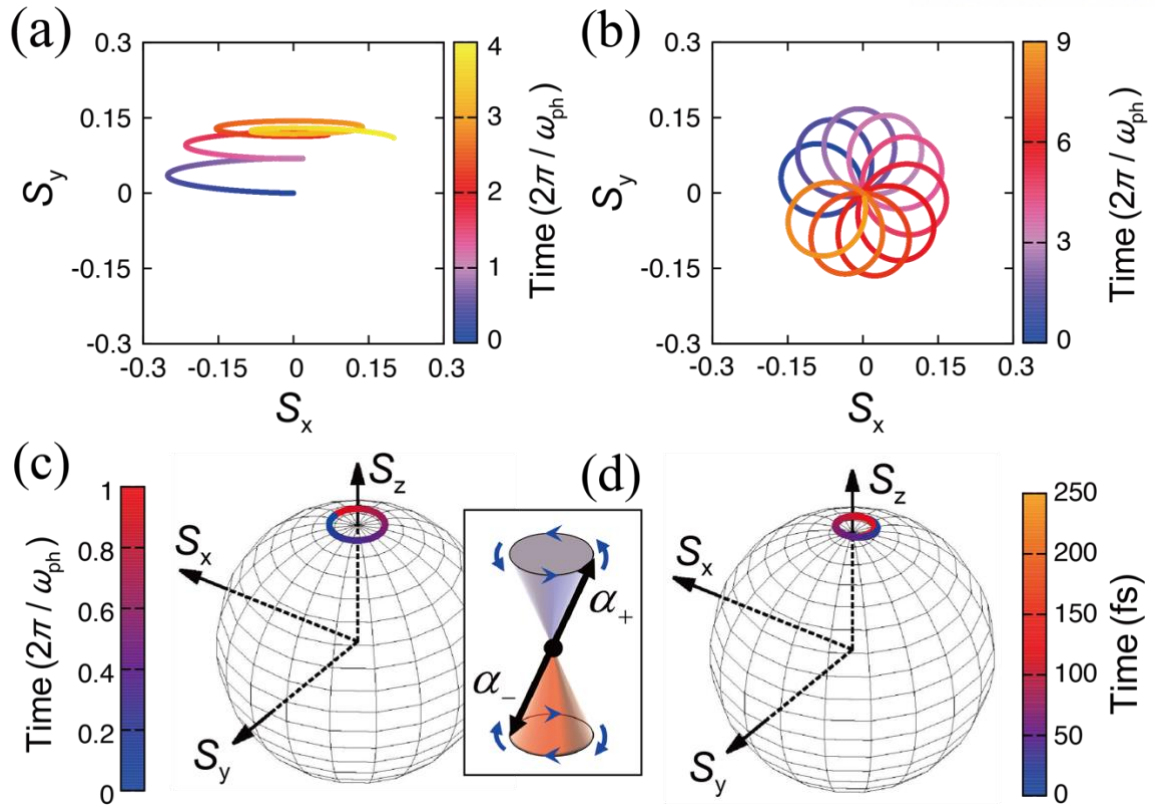
Figure 3-3. The spin trajectory calculated by model Hamiltonian with (a) linearly polarized and (b) circularly polarized magnetic field. The Floquet eigenstate calculated by (c) model Hamiltonian and (d) TDDFT. The inset of (c) show the Floquet eigenstates.

3.4. Simplified model Hamiltonian and Floquet eigenstates

From the results of TDDFT and DFT calculations, the simplified model Hamiltonian is set to mimic the spin dynamics of CBM valley state with coherent E`` phonon mode:

$$\hat{H}(t) = \varepsilon_0 \hat{\sigma}_z + \varepsilon_{ph} \hat{\sigma}_y \sin(\omega_{ph} t) \quad (3\text{-}1)$$

where ε_0, ε_{ph}, ω_{ph} and $\hat{\sigma}$ are intrinsic spin splitting gap, phonon induced spin splitting gap, E`` phonon frequency and Pauli matrix, respectively. This model Hamiltonian has two terms that first is the intrinsic SOC interaction along the out-plane direction and second term is the oscillating effective magnetic field induced by E`` phonon mode along the y-direction. With this simplified model Hamiltonian, the time propagation of spinor states is investigated. To solve this model Hamiltonian numerically, we determined the coefficients of model Hamiltonian from the calculation results of the band structure with atomic displacement and time profile of spin dynamics of CBM valley state. When the phonon induced spin splitting gap (ε_{ph}) is three times higher than intrinsic gap ($\varepsilon_{ph} = 3\varepsilon_0$), the initially spin-down state ($S_z(t=0) = -0.5\hbar$) shows dramatical spin-trajectory as shown in Figure 3-3a. In addition, this calculation result shows similar spin trajectory as TDDFT calculation with given initial kinetic energy ($E_{kin} = 13 meV$) (see Figure 3-1c). It indicates that this simplified model Hamiltonian well describes the spin dynamics of CBM valley under the effect of E`` phonon mode.

The effect of circularly polarized E`` phonon mode on the spin state of CBM valley is also investigated under the model Hamiltonian study. The simplified model Hamiltonian, which describes the spin state of CBM valley with right-handed circularly polarized phonon, is written as

$$\hat{H}(t) = \varepsilon_0 \hat{\sigma}_z + \varepsilon_{ph} \left(\sin(\omega_{ph} t) \hat{\sigma}_x + \cos(\omega_{ph} t) \hat{\sigma}_y \right). \quad (3\text{-}2)$$

With initial spin down state ($|\Psi(0)\rangle = \begin{pmatrix} 0 \\ 1 \end{pmatrix}$), the analytical solution of the spin dynamics for Eq. 3-2 is written as

$$|\Psi(t)\rangle = \begin{pmatrix} -i e^{i\frac{\omega_{ph}}{2}t} \dfrac{\varepsilon_{ph}}{\hbar \Omega_R} \sin(\Omega_R t) \\[2ex] e^{-i\frac{\omega_{ph}}{2}t} \dfrac{i\Delta_R \sin(\Omega_R t) + \Omega \cos(\Omega_R t)}{\Omega_R} \end{pmatrix}, \quad (3\text{-}3)$$

where $\Delta_R = \dfrac{\omega_{ph}}{2} + \dfrac{\varepsilon_0}{\hbar}$ and $\Omega_R = \sqrt{\Delta_R^2 + \left(\varepsilon_{ph}/\hbar\right)^2}$. This spin trajectory of CBM valley state shows double circularly rotating shape as shown in Figure 3-3b. When the Hamiltonian has time periodicity

$(T = \dfrac{2\pi}{\omega_{ph}})$, the time-dynamics can be decomposed into Floquet eigenstate $|\Psi_\alpha\rangle = e^{-i\alpha t}|\Phi_\alpha\rangle$, which

satisfies following equation

$$\left[\hat{H}(t) - i\hbar\frac{\partial}{\partial t}\right]|\Phi_\alpha\rangle = \alpha|\Phi_\alpha\rangle, \text{ with } |\Phi_\alpha(t)\rangle = |\Phi_\alpha(t + 2\pi/\omega_{ph})\rangle. \text{ (3-5)}$$

The Floquet analysis can provide simple picture of time periodic dynamics. The analytical solution of Floquet eigenstates of Eq. 3-2 is written as

$$|\Psi_{\alpha_+}\rangle = e^{-i\alpha_+ t}|\Phi_{\alpha_+}\rangle = \frac{\varepsilon_{ph}/\hbar}{\sqrt{2\Omega(\Omega - \Delta_R)}}e^{-i\left(\frac{\omega_{ph}}{2} + \Omega\right)t}\begin{pmatrix} e^{i\omega_{ph}t} \\ \dfrac{\Omega - \Delta_R}{\varepsilon_{ph}/\hbar} \end{pmatrix}, \text{ with } \alpha_+ = \frac{\omega_{ph}}{2} + \Omega.$$

$$(3\text{-}6)$$

$$|\Psi_{\alpha_-}\rangle = e^{-i\alpha_- t}|\Phi_{\alpha_-}\rangle = \frac{\varepsilon_{ph}/\hbar}{\sqrt{2\Omega(\Omega + \Delta_R)}}e^{-i\left(\frac{\omega_{ph}}{2} - \Omega\right)t}\begin{pmatrix} -e^{i\omega_{ph}t} \\ \dfrac{\Delta_R + \Omega}{\varepsilon_{ph}/\hbar} \end{pmatrix}, \text{ with } \alpha_- = \frac{\omega_{ph}}{2} - \Omega.$$

The spin-trajectories of these Floquet eigenstates show simple Larmor precessions with opposite direction as shown in Figure 3-3c. The linear combination of these Floquet eigenstates $(|\Psi(t)\rangle = c_+|\Psi_{\alpha_+}(t)\rangle + c_-|\Psi_{\alpha_-}(t)\rangle)$ describes the all spin-trajectories governed by Hamiltonian in Eq (3-2) with given initial conditions. To verify the Floquet eigenstate of model Hamiltonian, the spin-trajectory of Floquet eigenstate calculated by time-evolution of CBM valley of monolayer MoS$_2$ with initial condition $|\psi_{KS}^{CBM}(t=0)\rangle = |\Psi_{\alpha_-}(t=0)\rangle$ as shown in Figure 3-4d. On the other hand, the left-handed circularly polarized phonon provides the different spin trajectory comparing with right-handed case as follows

$$|\Psi_{\alpha_+}\rangle = e^{-i\alpha_+ t}|\Phi_{\alpha_+}\rangle = \frac{\varepsilon_{ph}/\hbar}{\sqrt{2\Omega_L(\Omega_L - \Delta_L)}}e^{-i\left(\frac{\omega_{ph}}{2} + \Omega\right)t}\begin{pmatrix} e^{i\omega_{ph}t} \\ \dfrac{\Omega_L - \Delta_L}{\varepsilon_{ph}/\hbar} \end{pmatrix}, \text{ with } \alpha_+ = \frac{\omega_{ph}}{2} + \Omega_L.$$

$$(3\text{-}7)$$

$$|\Psi_{\alpha_-}\rangle = e^{-i\alpha_- t}|\Phi_{\alpha_-}\rangle = \frac{\varepsilon_{ph}/\hbar}{\sqrt{2\Omega_L(\Omega_L + \Delta_L)}}e^{-i\left(\frac{\omega_{ph}}{2} - \Omega\right)t}\begin{pmatrix} -e^{i\omega_{ph}t} \\ \dfrac{\Delta_L + \Omega_L}{\varepsilon_{ph}/\hbar} \end{pmatrix}, \text{ with } \alpha_- = \frac{\omega_{ph}}{2} - \Omega_L.$$

where $\Delta_L = \dfrac{\omega_{ph}}{2} - \dfrac{\varepsilon_0}{\hbar}$ and $\Omega_L = \sqrt{\Delta_L^2 + \left(\varepsilon_{ph}/\hbar\right)^2}$.

This result indicates that there are different spin trajectories between time-reversal partners under the circularly polarized phonon on the system.
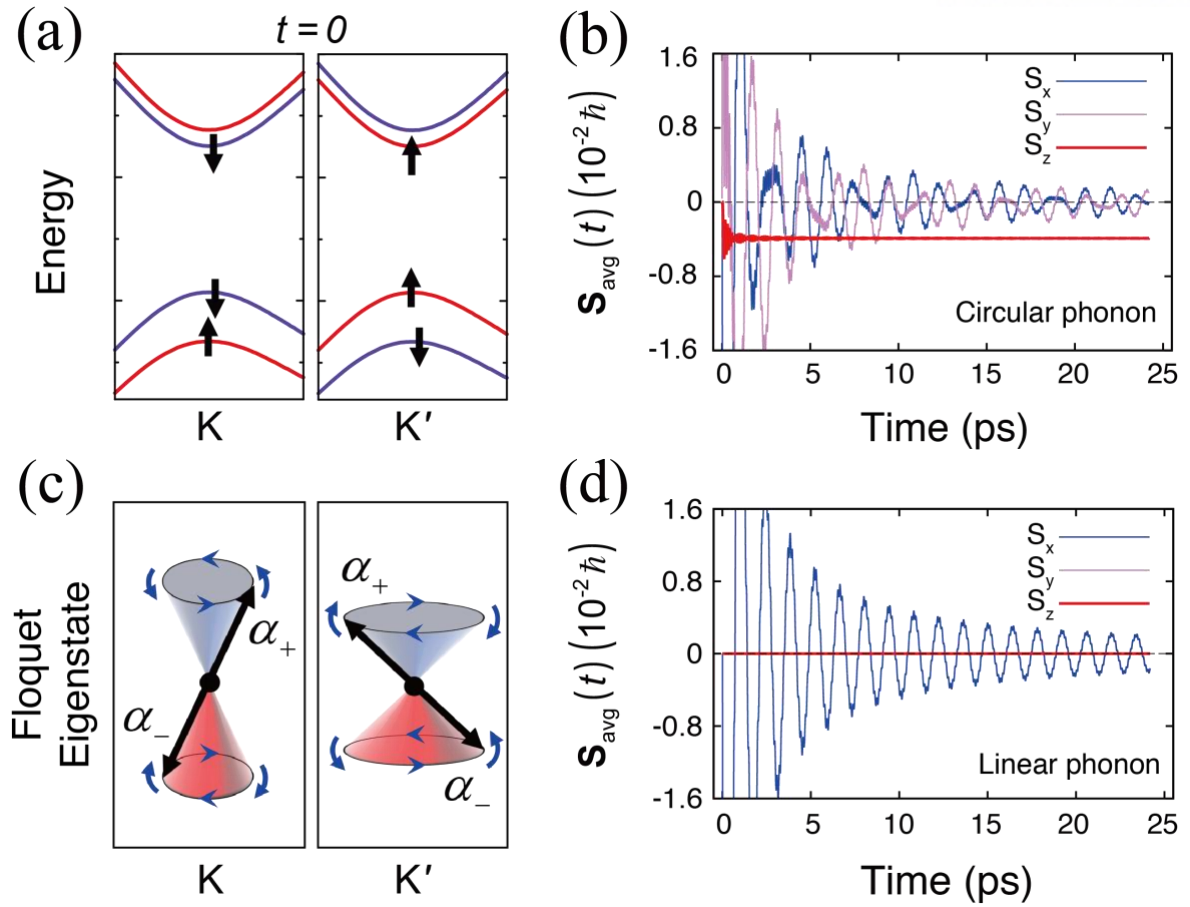
Figure 3-4. (a) Schematic time reversal symmetric charge carrier distribution at CBM valley. (b) Time profile of spin expectation value under the circularly polarized E'' phonon. (c) The spin-Floquet eigenstates at K and K′ induced by circularly polarized phonon. (d) Time profile of spin expectation value under the linearly polarized phonon.

3.5. Phonon-induced Valley magnetism in monolayer MoS₂

Based on the Floquet analysis, we found that the circularly polarized phonon provides the different spin motion between time-reversal pairs of CBM states in monolayer MoS_2. For an example, the shallow electron doped monolayer MoS_2 can be considered as shown in Figure 3-4a. There are two occupied spin polarized states at CBM valleys, which are spin down and spin up states at the K and K` points, respectively. The time propagation of these two states are proceed under the circularly polarized E`` phonon mode in Eq. 3-2. The time-reversal broken spin trajectories at K and K` points show the net non-zero spin $S_z$ value as shown in Figure 3-4b. This behavior can be easily clarified by Floquet analysis. With the same-helicity of circularly polarized phonon, spin state of CBM valleys at K and K` points suffer opposite helicity. For example, the spin trajectory of CBM state at K point follows Hamiltonian with the right circularly polarized light in Eq. 3-6, while CBM state at K` point follows Hamiltonian with the left circularly polarized light in Eq. 3-7. Considering the S_z expectation value for Floquet eigenstate is given as

$$\left\langle \Psi_{\alpha_+}(t) \middle| \hat{S}_z \middle| \Psi_{\alpha_+}(t) \right\rangle = \hbar \Big/ \left(2\sqrt{1 + \varepsilon_{ph}^2 / \Delta^2} \right), \quad (3\text{-}8)$$

the Floquet eigenstates at K and K` points show different S_z value as shown in Figure 3-4c. As a result, this time-reversal symmetry breaking induces the non-zero net spin magnetism. On the other hand, the linearly polarized phonon keeps time-reversal symmetry and provides time-averaged zero net out-plane spin magnetism as shown in Figure 3-4d.

TMDCs	$\Delta E_{VBM,spin-split}$	$\Delta E_{CBM, spin-split}$	E'' phonon
CrS_2	70 meV	3.6 meV	7.8 THz
$CrSe_2$	92 meV	16 meV	4.4 THz
$CrTe_2$	109 meV	21 meV	3.1 THz
MoS_2	150 meV	3 meV	8.2 THz
$MoSe_2$	188 meV	20 meV	4.8 THz
$MoTe_2$	219 meV	32 meV	3.3 THz
WS_2	440 meV	28 meV	8.5 THz
WSe_2	481 meV	34 meV	4.9 THz
WTe_2	504 meV	48 meV	3.4 THz

Table 3-1 The spin splitting gap of VBM and CBM states, and the E'' phonon frequencies of various TMDCs.
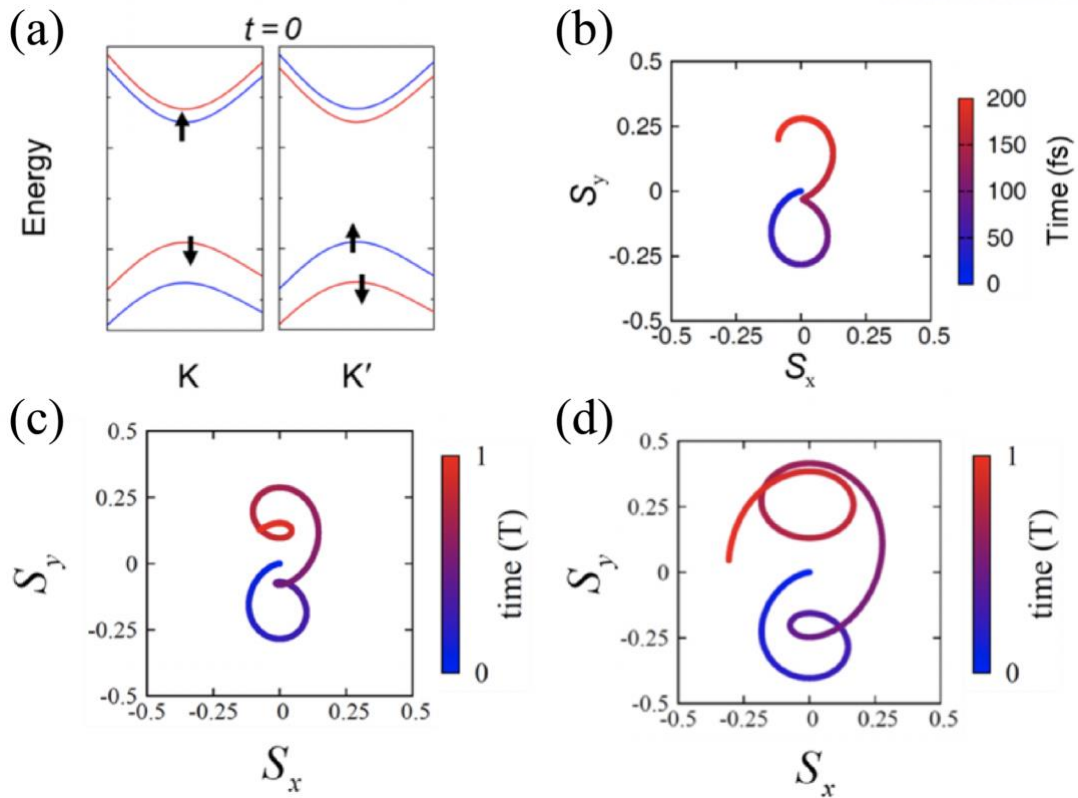
Figure 3-5. (a) The initial carrier distribution for one electron excited state at the K valley of monolayer WTe$_2$. Time-profile of spin expectation value of CBM state at K point calculated by (b) TDDFT and (c) model Hamiltonian with zero phonon energy ($\frac{1}{2}\hbar\omega_{ph}$). (d) Time-profile of spin expectation value of CBM state at K point calculated by model Hamiltonian with single phonon energy ($\frac{3}{2}\hbar\omega_{ph}$).

3.6. Spin-phonon interaction in other TMDC materials

Up to now, monolayer MoS_2 is employed to understand the phenomena of effect of E`` phonon on CBM valley. Through the Floquet analysis in Eq. 3-8, we found that the higher CBM spin splitting gap provides the larger phonon-induced Floquet magnetic moment. To find the best candidate material for experimental observation of this Floquet magnetism, various TMDC species are considered. The spin splitting gap of VBM and CBM valleys and phonon frequency of E`` mode for TMDCs are summarized in Table 3-1. Among them, monolayer WTe_2 provides the highest spin splitting gap of CBM valley, and I expected that the monolayer WTe_2 shows highest value of phonon-induced magnetic moment.

To investigate the phonon-induced magnetism in monolayer WTe_2, the real-time spin dynamics of CBM valley is simulated with y-direction linearly polarized E`` phonon using TDDFT calculation. For the initial condition at t=0, the spin up CBM state at K valley is occupied by excitation as shown in Figure 3-5a and the atomic velocity is set toward the eigenvector direction of E`` phonon with zero-phonon energy ($E_{kin}^{atom}(t=0) = \frac{1}{2}\hbar\omega_{ph}$). The real time dynamics of monolayer WTe_2 system is calculated by TDDFT. The time-profile of spin state is shown in Figure 3-5b. By comparing with this calculation result and model Hamiltonian in Eq. 3-1, the strength of effective magnetic field induced by E`` phonon mode ($\varepsilon_{ph} = 0.44\varepsilon_0$) is evaluated as shown in Figure 3-5c. The effect of single phonon quanta ($E_{kin}^{atom}(t=0) = \frac{3}{2}\hbar\omega_{ph}$) is also considered, and we found that stronger effective magnetic field strength ($\varepsilon_{ph} = 0.75\varepsilon_0$) is induced by more phonons as shown in Figure 3-5d.
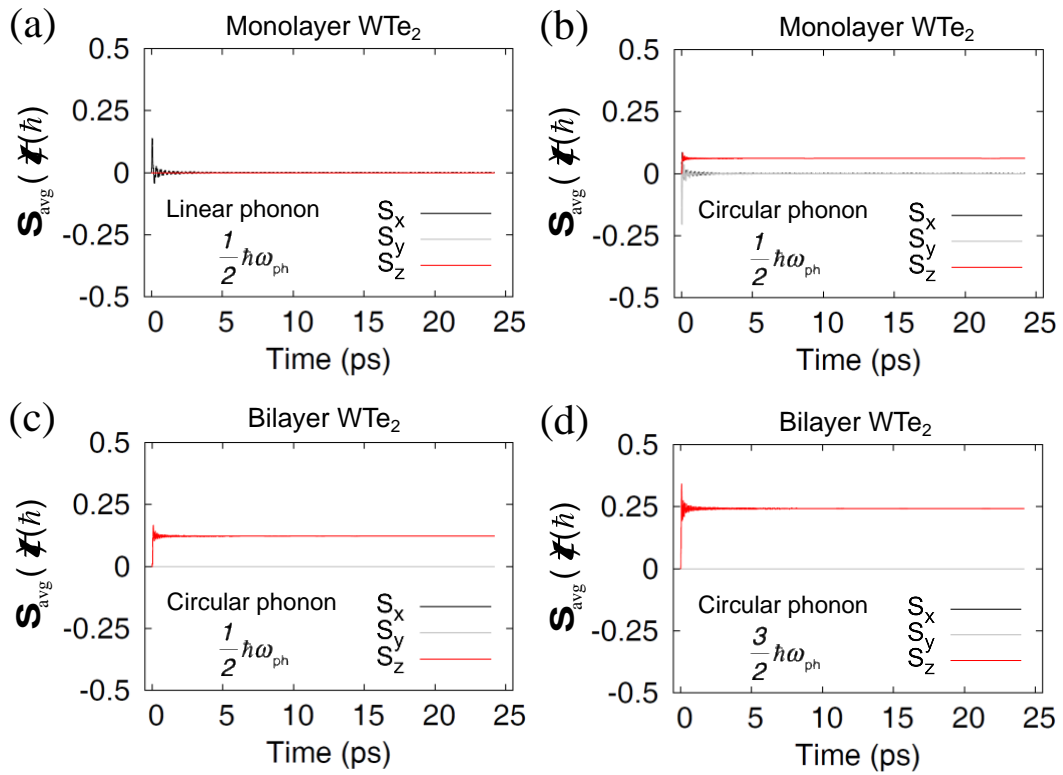
Figure 3-6 The cumulative time average of the total spin in monolayer WTe$_2$ induced by (a) linear and (b) circular polarized E'' phonon. The same total spin of the bilayer WTe$_2$ with a circular polarized E_u phonon energy with (c) zero-point phonon ($\frac{1}{2}\hbar\omega_{ph}$) and (b) single phonon ($\frac{3}{2}\hbar\omega_{ph}$).

3.7. Phonon-induced magnetism in monolayer WTe$_2$ and bilayer WTe$_2$

The Floquet magnetism in monolayer WTe$_2$ induced by phonon is investigated in the time-reversal symmetric carriers of CBM valleys as a good experimental candidate material. As similar as monolayer MoS$_2$ case, it is found that the expected net spin magnetic moment induced by linearly polarized phonon with zero phonon energy is negligible in monolayer WTe$_2$ system as shown in Figure 3-6a. On the other hand, the circularly polarized phonon induces the non-zero spin magnetic moment as shown in Figure 3-6b. Comparing with the induced spin magnetic moment in monolayer MoS$_2$ ($S_{avg} = 0.0078 \mu_B$), monolayer WTe$_2$ shows higher value ($S_{avg} = 0.06 \mu_B$) with zero-phonon quanta. It is consistent with the result of Floquet analysis that the larger spin splitting gap provides the higher phonon induced magnetic moment value.

The last stage for the experimental observation is the generation of coherent circularly polarized E`` phonon. The E`` phonon in monolayer TMDC is infra-red (IR) in-active mode, it means that the experimental generation of coherent E`` phonon is impossible. However, bilayer WTe$_2$ has the IR active E$_u$ phonon mode, which mode is two alternating E`` phonon mode between AB stacked bilayer WTe$_2$. The effect of E$_u$ phonon mode on the time-reversal four CBM valleys is evaluated using model Hamiltonian study. It is found that circularly polarized E$_u$ phonon mode of bilayer WTe$_2$ provides enhanced induced magnetic moment value $S_{avg} = 0.12 \mu_B$ with zero-phonon quanta and $S_{avg} = 0.24 \mu_B$ with single-phonon quanta as shown in Figures 3-6c and 3-6d. This result indicates that the bilayer WTe$_2$ is most promising candidate material for experimental observation of the phonon induced magnetization.

3.8. Conclusion

In this study, the effect of coherent phonon mode on the spin state of CBM valley in monolayer MoS_2 is investigated. The time-profile of spin dynamics reveals that coherent $E``$ phonon mode induces the significant variation of spin state at CBM valley by generating effective magnetic field. In addition, I found that the circularly polarized phonon can induce non-zero spin magnetic moment in the time-reversal symmetric system. It is also verified that the other monolayer TMDC species show the same spin-phonon interaction. Especially, I suggested that the bilayer WTe_2 is the best candidate for the experimental observation of phonon-induced magnetism.

Ⅳ. Revelation of band topology in time propagating Bloch state

4.1. Berry curvature and topological classification in condensed matter

The adiabatic transition of state along the closed loop generates the additional phase (called Berry phase) [27]. Recent few decades, a property of Berry phase has been investigated in various field of physics. In the condensed matter physics, the electrons in periodic potential is characterized by Bloch vector ($\vec{k}$) which can be a geometrical parameter of reciprocal space [28]. When the electron adiabatically travels a closed loop of Brillouin zone (BZ), it obtains the Berry phase depending on the transition path. This effect of the Berry phase can be written in a local gauge-invariant field tensor form (called Berry curvature ($\Omega_{\vec{k}}$)). The non-zero Berry curvature acts like an external magnetic field in the material. By applying a static E-field, for example, it occurs anomalous velocity of Bloch state as follows $v_{\vec{k}} = \dfrac{\partial \varepsilon_{\vec{k}}}{\hbar \partial \vec{k}} - \dfrac{e}{\hbar} \vec{E} \times \Omega_{\vec{k}}$. Especially, inversion symmetry broken honeycomb lattice system shows the opposite value of Berry curvatures between time-reversal partners points. Utilizing this characteristic of material, application devices are suggested in several studies [29].

The topological classification of quantum Hall state is firstly identified by Thouless, Kohmoto, Nightingale and Nijs (TKNN) [30]. They reveal that quantized Hall conductivity is identical to mathematically defined geometrical class (called Chern number *n*). This study ignites the discovery of topological material without net non-zero magnetic field. In 1988, Haldane shows that graphene system with alternating magnetic flux induces band gap at Dirac points with non-zero Chern number, while net magnetic flux is zero on the entire system [31]. Few decades later, Kane and Mele proves that two copies of Haldane's model in time reversal symmetry can exist in graphene system with the strong spin-orbit coupling interaction [32]. Bernevig, Hughes and Zhang also show the same time reversal symmetric topological state in quantum well structure. This topological phase of material is called quantum spin Hall state [33]. Because time-reversal symmetric system always shows zero Chern number (*n*=0), new identification of topological class for this state is required. Unlike a clear definition of charge Hall conductivity, the non-conserved spin texture gives a suspicion of evaluation of quantized spin Hall conductivity using linear response methods [32, 34]. Instead of classification defined by physical observable origin, Z_2 topological identification is employed to analyze the band topology [34]. Recently, the topological phase transition by external perturbation is suggested, such as light [35]. On the other hand, it is doubtable that the topological class of material is well identified by the linear response methods with non-equilibrium carrier distribution.

In this study, the band topology and Berry curvature are evaluated by the time-propagation of KS state. With trivial insulators, the transport properties of Bloch state, such as Bloch oscillation and anomalous velocity, are investigated. As a second example, the transverse conductivity of quantum anomalous Hall insulator is evaluated from the Brillouin zone integration of anomalous velocity under

the static E-field. Finally, the quantized spin Hall conductivity is calculated in quantum spin Hall insulators. These studies indicate the Berry curvature and topological property are well exposed by the expectation value of velocity of time-propagating Bloch states and can extend to evaluate the topological phase of non-equilibrium state.
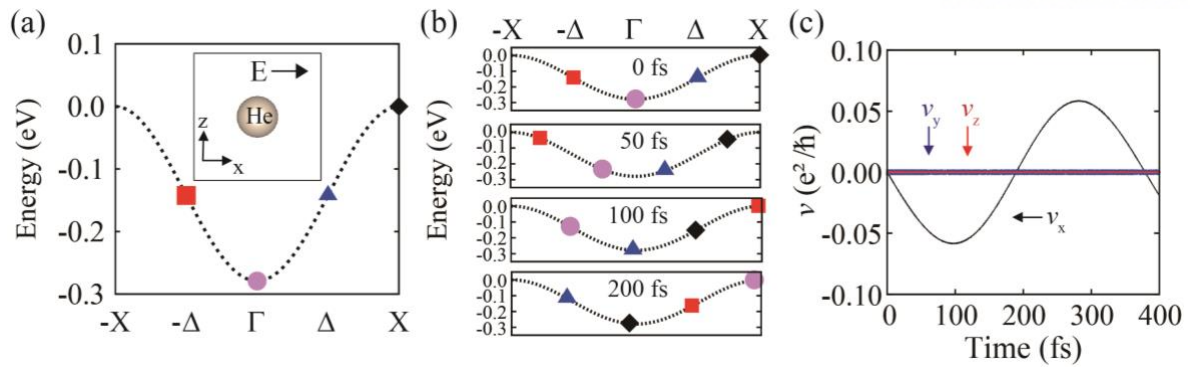
Figure 4-1. Time propagation of a Bloch band of a three-dimensional trivial insulator in response to an applied E-field. (a) The band structure of the solid cubic He. (b) Time profile of the band energy of four selected Bloch states. (c) Time profile of longitudinal (v_x) and transverse velocities (v_y and v_z) of the Bloch state starting from Γ point. Inset of (a) shows the unit cell with the direction of the E-field. In (a) and (b), the four selected Bloch states are denoted by the symbol of square, circle, triangle, and diamond.

4.2. Bloch oscillation in cubic He solid

The study of time-propagating Bloch state under the static E-field is started with trivial atomic insulator. As a gedanken system, the cubic He atomic insulator is employed as shown in inset of Figure 4-1a. With lattice constant $a_0 = 3$ Å, this system has wide band gap (16.5 eV) and single occupied $1s$ band with 0.28eV band dispersion as shown in Figure 4-1a. The static E-field is applied along x-direction with field strength $\vec{E} = 3.7 \times 10^{-3} \hat{x}$ V/Å and specific Bloch states are traced; $\vec{k} = -\Delta(-0.25, 0, 0)$, $\Gamma(0,0,0)$, $\Delta(0.25, 0, 0)$, and $X(0.5, 0, 0)$ in the unit of $b_0 = 2\pi/a_0$. The time profies of band energy ($\varepsilon_{\vec{k}}(t) = \left\langle \psi_{\vec{k}}(t) \middle| \hat{H}(t) \middle| \psi_{\vec{k}}(t) \right\rangle$) are shown in Figure 4-1b. Under the static E-field, I found that the band energy of Bloch states follow the band dispersion of ground state under the relation between Bloch vector and static E-field $\vec{k}(t) = \vec{k}_0 - e\vec{E}t/\hbar$. For example, the Bloch state starting from Γ point shows increament of band energy $\varepsilon_\Gamma(t)$ until the 200 fs following the band dispersion. The other Bloch state starting from X, Δ and -Δ points are also traking the adiabatic energy band dispersion. This result indicates that the Bloch states in wide band gap insulator show the adiabatic transition following the ground energy dispersion under the weak static E-field.

The velocity expectation value contains band dispersion and anomalous velocity terms as follows $\vec{v}_{n,\vec{k}}(t) = \dfrac{\partial \varepsilon_n(\vec{k},t)}{\hbar \partial \vec{k}} - \dfrac{e}{\hbar} \vec{E} \times \Omega_n(\vec{k},t)$ [28]. When the static E-field is applied on the system, the anomalous velocity can be generated by non-zero Berry curvature. However, there is negligible Berry curvature value in this cubic He solid insulator. The velocity expectation value of Bloch state in this system only describes the band dispersion $\dfrac{\partial \varepsilon_n(\vec{k},t)}{\hbar \partial \vec{k}}$ term. The time profile of velocity expectation value for Bloch state starting from Γ point is shown in Figure 4-1c. The longitudinal velocity $v_x(t)$ against the applying E-field direction shows oscillation with time period $T = b_l \hbar / eE_0 = 375 fs$, while there are negligible variation on transverse velocity $v_y(t)$ and $v_z(t)$. This time periodicity of velocity expectation value is originated from the periodicity of Brillouin zone, which phenomena is known as Bloch oscillation [36].
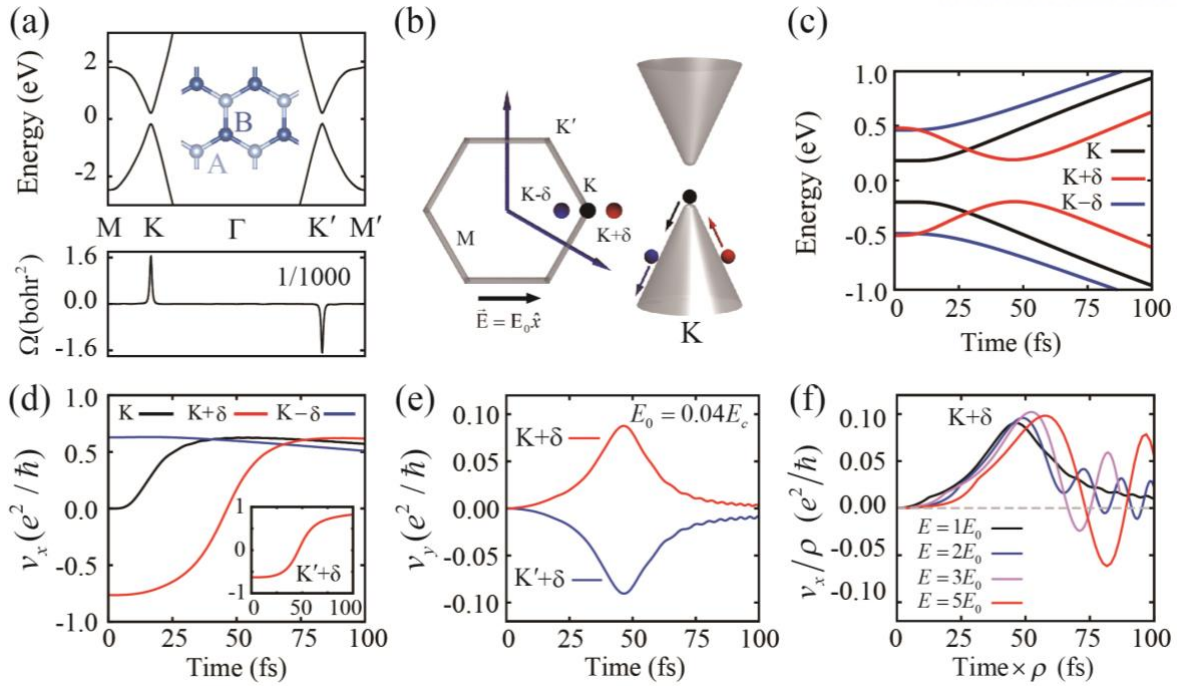
Figure 4-2. (a) Band structure (upper panel) and Berry curvature (lower panel) of inversion symmetry broken graphene. (b) Schematics of the Brillouin zone and the Dirac cone with three selected k-points in the K valley of the BZ. (c) Time profile of band energies of the VBM and CBM states at the specified three k-points in K valley. (d) Time profile of the longitudinal velocities of the states of three k-points in K valley. Inset shows the same longitudinal velocity of K′+δ point. (e) Time profile of the transverse velocity of the states starting from the K+δ and K′+δ points. (f) The same as (e) for the state starting from K+δ point with various strength of the E-field: $E = \rho E_0$. Here, E_0 indicates the strength of the E-field used for (c)(d)(e). In the inset of (a), atomic symbols schematically depict the inversion-broken sublattices of two C atoms by Hubbard U potential.

4.3. Valley Hall system: inversion symmetry-broken graphene

The pristine graphene has two Dirac points at K and K` points in the Brillouin zone. When inversion symmetry of graphene is broken by perturbation, band gap and Berry curvature are developed at the Dirac points. In this study, the inversion symmetry broken graphene is constructed by applying the Hubbard U potential on the *p*-orbital of single Carbon atom site A ($U = 4eV$) as shown in inset of Figure 4-2a. As a result, band gap (0.38eV) and locally non-zero Berry curvature are developed at K and K` points as shown in Figure 4-2a. This non-zero Berry curvatures at K and K` points show opposite value ($\Omega(\vec{k}) = -\Omega(-\vec{k})$) by time reversal symmetry. To investigate the real-time dynamics of Bloch states with non-zero Berry curvature, the static E-field along the x-direction is applied $\vec{E} = E_0\hat{x} = 1.45\times10^{-3}\hat{x}$ *V/Å* and responses of specific Bloch states near the K point are traced; K, K+δ, and K-δ with $\delta = 0.03\frac{2\pi}{a_0}\hat{x}$ as shown in Figure 4-2b. The time profiles of band energy of these specific Bloch states are shown in Figure 4-2c. The band energies of valence band state starting from K (black) and K-δ (blue) points decreases following the Dirac cone by static E-field along the positive direction as shown in Figure 4-2b (right). On the other hand, the band energy of valence band state starting from K+δ (red) point increases up to 47fs by claiming the Dirac cone and decreases after that time by going downhill on the Dirac cone. This result indicates that the Bloch states follows the adiabatic energy surface of Dirac cone during the time propagation.

The time profile of longitudinal velocities of three Bloch states indicate the group velocity along x-direction ($\frac{\partial\varepsilon}{\partial\vec{k}_x}$) as shown in Figure 4-2d. After the 75fs, longitudinal velocity of three Bloch states converse the same value of slope of Dirac cone. In addition, the Bloch state starting from K`+δ point shows the similar time-profile of velocity as K+δ point as shown in inset of Figure 4-2d. By non-zero Berry curvature of this system, on the other hand, applying the static E-field along the x-direction develops the anomalous velocity ($-e\vec{E}\times\Omega(\vec{k})$) along y-direction direction. The transverse velocities of Bloch states starting from the K+δ (red) and K`+δ (blue) are shown in Figure 4-2e. When these two points reach the top of the Dirac cone at 47 fs, the amplitude of transverse velocities are maximized by the highest value of local Berry curvature. This result indicates that the anomalous velocity is explicitly described by expectation value of velocity of time propagating Bloch state.

In addition, I investigate the adiabaticity of time-propagating Bloch state under the strong static E-field. The electronical breakdown of semiconductor can be occurred by transition between conduction and valence band under the strong E-field, which phenomena is known as Zener tunneling. The probability of Zener tunneling is given by terms of E-field strength and band gap ($\exp\left(-\frac{\pi m_r^{1/2}\Delta_{gap}^{3/2}}{2\hbar E}\right)$).

35

The critical field strength can be estimated as follows $E_c = \dfrac{\pi}{2\hbar}\sqrt{m_r \Delta_{gap}^3}$. To investigate the effect of strong static E-field on the Bloch state, we applied various strengths of E-field on the Bloch state in the inversion symmetry broken graphene; E_0, $2E_0$, $3E_0$ and $5E_0$ while $E_0 = 0.04 E_c$. I found that the stronger static E-field strength induces the oscillation of transverse velocity with higher amplitude as shown in Figure 4-2f. On the other hand, the field strength under the $0.04 E_c$ keeps the adiabatic transition as shown in Figure 4-2c to 4-2e. It is noteworthy that the non-equilibrium excited dynamics and adiabatic transition can be both evaluated using TDDFT calculation.
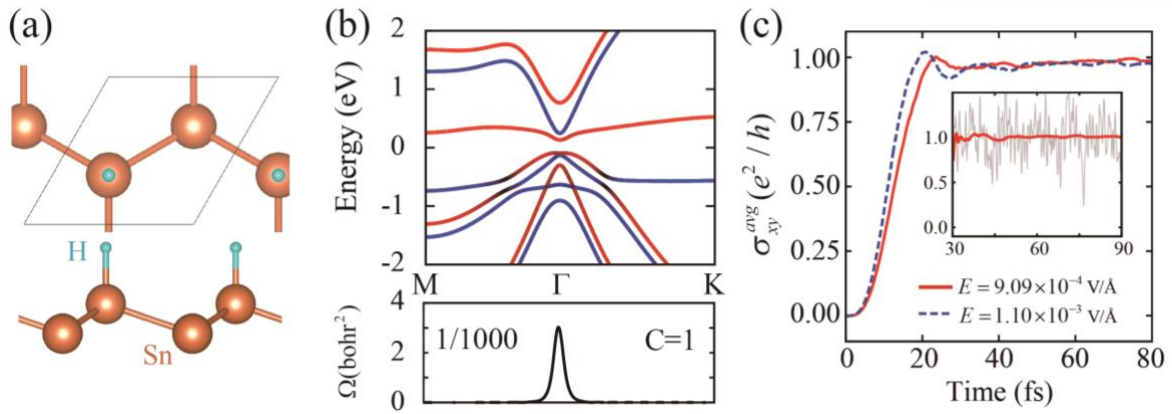
Figure 4-3. (a) Atomic geometry, (b) band structure and Berry curvature, and (c) the time-averaged Hall conductivity. Red and blue lines in (b) indicate the positive and negative spin state polarized along the z-direction, respectively. The inset of (c) shows the time profile (gray) and the time-averaged profile (red) of the Hall conductivity after the adiabatic turn-on.

4.4. Quantum anomalous Hall insulator

In 1988, D. Haldane shows the Chern insulator, so called quantum anomalous Hall insulator, can be formed in graphene system under the net zero magnetic flux [31]. This quantum material is found at the system has single spin sector band inversion by strong spin orbit coupling interaction [37, 38]. Recent theoretical study revealed that the half halogenated monolayer Sn is quantum anomalous Hall insulator by band inversion of ferromagnetic ordered *p*-orbitals of Sn. To investigate the effect of static E-field on the quantum anomalous Hall system, the half hydrogenated monolayer Sn is employed which atomic geometry is shown in Figure 4-3a. This system shows BHZ-type single spin sector band inversion at the Γ point. The Berry curvature and quantized Hall conductivity ($\sigma_{xy} = \dfrac{e^2}{h}$) calculated by Kubo formular are shown in figure 4-3b [37]. To trace the time profile of Hall conductivity in this system, time evolution of Bloch states is proceeded using TDDFT method. The static E-field $\vec{E} = 1.10 \times 10^{-3} \hat{y}$ *V/Å* is applied on the system with adiabatic turn-on duration (20 fs). The Hall conductivity of the system is evaluated by the summation of transverse velocity around Brillouin zone as follows

$$\sigma_{xy}(t) = \frac{J_y}{E_x} = -\frac{1}{mE_x} \sum_{n,\vec{k}} \left\langle \psi_{n,\vec{k}}(t) \left| \hat{\pi}_y \right| \psi_{n,\vec{k}}(t) \right\rangle \quad (4\text{-}1)$$

The time-averaged Hall conductivity ($\sigma_{xy}^{avg}(t) = \dfrac{1}{t} \int_0^t \sigma_{xy}(\tau) d\tau$) indicates the quantized Hall conductivity of half hydrogenated monolayer Sn as shown in Figure 4-3c.
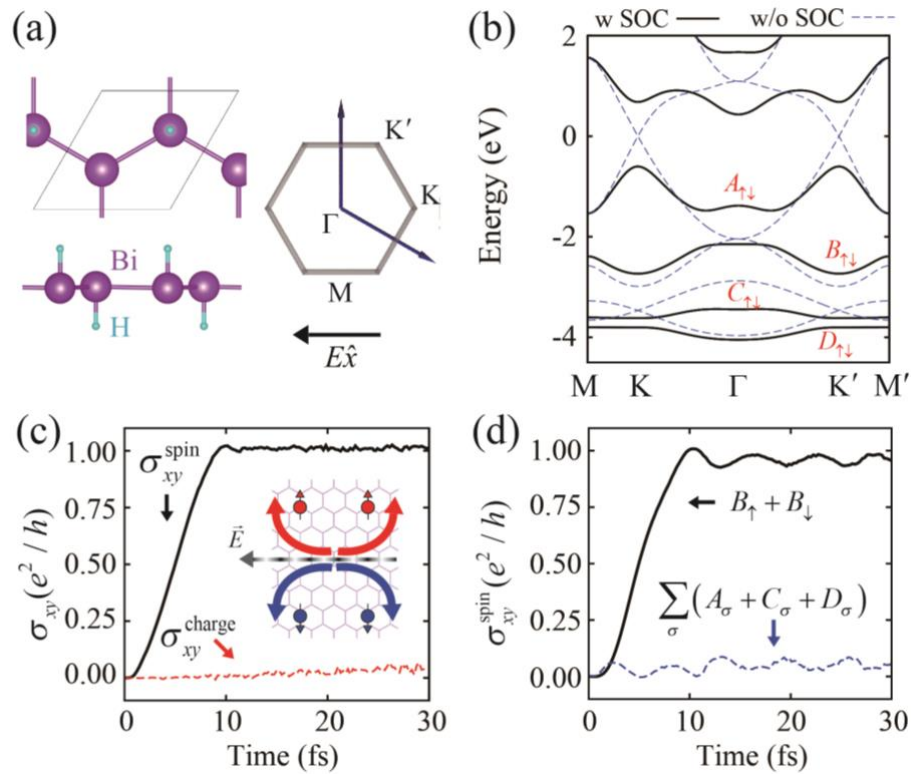
Figure 4-4. (a) Schematics of the geometry and the Brillouin zone of fully hydrogenated Bi. (b) Band structures with (solid line) or without (dashed line) spin orbit coupling interaction term. Doubly degenerate valence bands are labeled A to D from the highest band. (c) Spin Hall and charge Hall conductivity calculated from the time-evolving Bloch states under the static E-field. (d) The band-resolved spin Hall conductivity from degenerated second valence band (B) and from the rest ($A+C+D$). Inset of (c) depicts the bias E-field and the spin current.

4.5. Quantum spin Hall insulator

By presence of strong spin-orbit coupling interaction, the quantum spin Hall effect is firstly suggested in graphene structure. The electronic structure of this material consists of two inversely paired Chern insulator under the time reversal symmetry [32]. As a result, quantized spin Hall conductivity $\sigma_{xy}^{spin} = 0.5\left(\sigma_{xy}^{\uparrow} - \sigma_{xy}^{\downarrow}\right) = e^2/h$ is formed, while there is zero charge Hall conductivity. The definition of this topological state is closely related with study of TKNN [30], but the degenerated spin state by time reversal symmetry makes it hard to compute the quantized spin Hall conductivity using linear response approach. In this study, I tried to evaluate the quantum spin Hall conductivity from the spin velocity expectation value of Bloch state under the static E-field using TDDFT. As an exemplary system of quantum spin Hall insulator, the full hydrogenated Bi is employed. The atomic geometry and the first BZ of this system are shown in Figure 4-4a. By comparing the band structure with and without spin-orbit coupling interaction term, the band inversion induced by strong spin-orbit coupling term is identified at K and K` points as shown in Figure 4-4b. Because of time reversal symmetry, each band is double degenerated by spin up and spin down states.

By applying the E-field strength $\vec{E} = 3.37 \times 10^{-6}\hat{x}$ *V/Å* with adiabatic turn-on duration 10fs, the time profile of spin Hall conductivity in the full hydrogenated Bi system is evaluated from the expectation value of spin velocity;

$$\sigma_{xy}^{spin}(t) = -\frac{1}{E_x}\sum_{n,\vec{k}}\left\langle\psi_{n,\vec{k}}(t)\left|\hat{j}_y^{s_z}\right|\psi_{n,\vec{k}}(t)\right\rangle = -\frac{1}{2mE_x}\sum_{n,\vec{k}}\left\langle\psi_{n,\vec{k}}(t)\left|\left\{\hat{S}_z,\hat{\vec{\pi}}_y\right\}\right|\psi_{n,\vec{k}}(t)\right\rangle \quad (4\text{-}2)$$

The quantized spin Hall conductivity is rapidly conserved after the adiabatic turn-on period, while the charge Hall conductivity evaluated by Eq. 4-1 is negligible as shown in Figure 4-4c. It is noteworthy that the non-conserved spin states near band inversion points provide the quantized spin Hall conductivity, while the linear response evaluation of spin Berry curvature doesn't show quantized value ($\sigma_{xy}^{spin} = 0.75e^2/h$) by them. Unlike the result of linear response with this non-conserved spin texture [32, 34, 39], quantized spin Hall conductivity evaluated from time propagation originates from the property of unitary operation in expectation value. The unitary operation on the spin state doesn't disturb the expectation value given as

$$\frac{1}{2}\sum_{n,\vec{k}}\left\langle\psi_{n,\vec{k}}(t)\left|\left\{\hat{S}_z,\hat{\vec{\pi}}_y\right\}\right|\psi_{n,\vec{k}}(t)\right\rangle = \frac{1}{2}\sum_{\vec{k}}\sum_{n}\left\langle\psi_{n,\vec{k}}(t)\left|\hat{U}_{\vec{k}}\left\{\hat{S}_z,\hat{\vec{\pi}}_y\right\}\hat{U}_{\vec{k}}^{-1}\right|\psi_{n,\vec{k}}(t)\right\rangle$$

$$= \sum_{\vec{k}}\frac{\hbar}{2}\left\langle\psi_{\uparrow,\vec{k}}(t)\left|\hat{\vec{\pi}}_y\right|\psi_{\uparrow,\vec{k}}(t)\right\rangle - \sum_{\vec{k}}\frac{\hbar}{2}\left\langle\psi_{\downarrow,\vec{k}}(t)\left|\hat{\vec{\pi}}_y\right|\psi_{\downarrow,\vec{k}}(t)\right\rangle \quad (4\text{-}3)$$

As a result, the expectation value of the spin Hall conductivity with non-conserved spin state can evalute

the quantized spin Hall conductivity of conserved spin state along the certain direction (e.g. S_Z).

As an extreme case of non-conserved spin texture, the fully hydrogenation Bi without inversion symmetry is considered as shown in Figure 4-5a. By the absence of inversion symmetry, the most spins of Bloch states are aligned along the in-plane direction as shown in Figure 4-5b. Under static E-field $\vec{E} = 3.37 \times 10^{-6} \hat{x}$ $V/\mathring{A}$ with adiabatic turn-on duration 10fs, the spin Hall conductivity is evaluated from time-propagation Bloch state. Same as inversion symmetric case, the quantized spin Hall conductivity is also calculated using Eq. (4-2). It is noteworthy that the expectation value of spin Hall conductivity evaluated from time-propagating Bloch state under static E-field reveals topological property of the system regardless of the spin states.
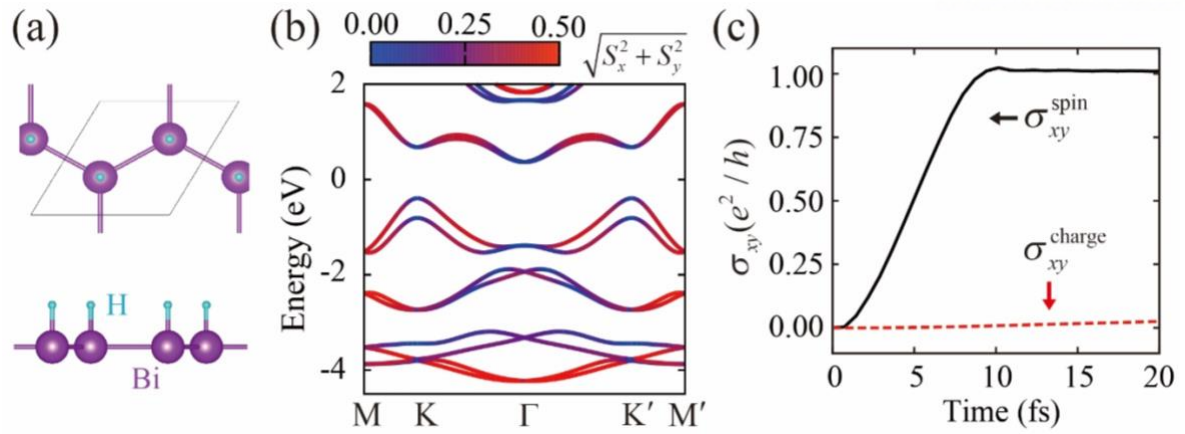
Figure 4-5. (a) Schematic geometry and (b) The spin resolved band structure of fully hydrogenated Bi. (c) Spin and charge Hall conductivity calculated by TDDFT. In (b), the color depicts the magnitude of the in-plane spin component.

4.6. Non-equilibrium dynamics; graphene nano-ribbon

Here, the non-equilibrium dynamics under the non-zero Berry curvature system is demonstrated which cannot be evaluated by the linear response approach. The example system is zigzag-edged graphene nano-ribbon (GNR). By applying static E-field ($\vec{E} = 1.68 \times 10^{-3} \hat{x}$ V/Å) along the ribbon axial direction, the current flow of one-dimensional (1-D) Bloch states is calculated using TDDFT. By the time-reversal symmetry of the system during the time propagation, there is absence of charge Hall current [29]. On the other hand, the charges accumulate on both edges by depleting the charge in the central of the ribbon as shown in Figure 4-6a. This result is come from the valley-Hall effect of the GNR. The electronic structure of zigzag-edged GNR has metallic band state and positive and negative non-zero Berry curvatures in the one-dimensional (1D) BZ which are come from zone-folding of graphene's two Dirac points (K and K′). Among 1D Bloch states, the states originated from the K and K′ valley provide the positive and negative anomalous velocities. As a result, the real space charges in GNR are transferred to both edge side under the static E-field.

Numerous previously studies reveal that time-reversal symmetry breaking by circularly polarized light can induce non-zero Hall current [40]. In the case of GNR, the presence of a circularly polarized light breaks the carrier distribution between the time-reversal pair K and K′ valleys. To simulate the simultaneous time-reversal symmetry breaking of GNR system, the velocity gauge form of circularly polarized light is described in time dependent KS Hamiltonian. Using TDDFT calculation, the current density of the 1-D Kohn-Sham bands is evaluated by applying static E-field along the axial direction ($\vec{E} = 3.6 \times 10^{-4} \hat{x}$ V/Å) and the circularly polarized E-field ($\vec{E} = 6.7 \times 10^{-4} (\hat{x} + i\hat{y}) e^{-i\omega t}$ V/Å and $\omega = 1 eV$). As a result, the carrier distribution in edge sides loses their symmetry and develops the charge Hall voltage across the ribbon width as shown in Figure 4-6b.
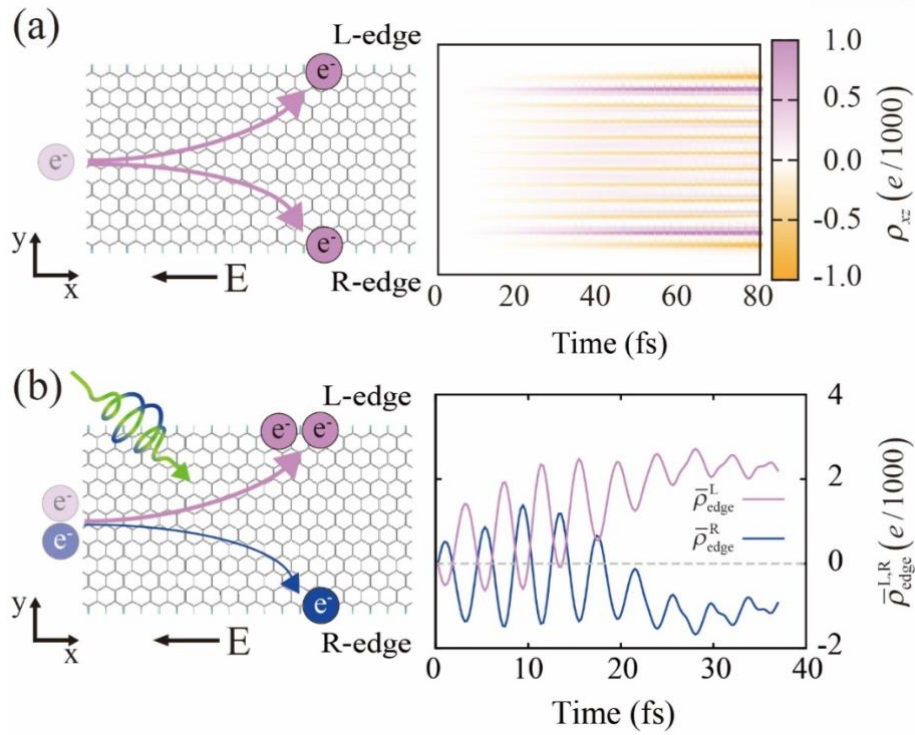
Figure 4-6. (a) Schematic of valley Hall effect (left) and the calculation results for the time-varying charge density in the graphene nano-ribbon. (b) The same as (a) but with a circularly polarized E-field in addition to the static axial bias. In (a) and (b), the time-varying charge density is obtained by $\rho_{xz}(y,t) = \iint dxdz\left[\rho(\vec{r},t) - \rho_0(\vec{r})\right]$, and $\bar{\rho}_{edge}^{L}$ and $\bar{\rho}_{edge}^{R}$ are the time-averaged charge obtained in each edge region of the ribbon (W=26Å): $\bar{\rho}_{edge}^{L}(t) = \frac{1}{t}\int_0^t d\tau \int_{0.8W}^{\infty} \rho_{xz}(y,\tau)dy$ and

$$\bar{\rho}_{edge}^{R}(t) = \frac{1}{t}\int_0^t d\tau \int_{-\infty}^{0.2W} \rho_{xz}(y,\tau)dy$$

4.7. Conclusion

In this study, I investigated the Berry curvature and band topology through the time-propagating Bloch states. The adiabatic transition and Bloch oscillation is observed in the time-propagating Bloch state of large band gap atomic insulator under the static E-field. The anomalous velocity induced by the local non-zero Berry curvature is also simulated in the inversion symmetry broken graphene system. The first two studies verified that the property of Bloch state related with periodicity of Brillouin zone and the Berry curvature is well described in the TDDFT scheme. In the last two examples, the quantized anomalous Hall conductivity and quantized spin Hall conductivity are evaluated from the velocity expectation value in the quantum anomalous Hall and quantum spin Hall insulator. It is noteworthy that the expectation value of transverse spin velocity leads to quantized spin Hall conductivity of topological insulator regardless of the spin texture.

Ⅴ. Long-range charge transfer in real-time dynamics

5.1. Introduction

The charge transfer is commonly happened between the chemical compound and material interface. For example, the charge transport between different electronegativity molecules makes the anion and cation molecules. In the catalysis processes, especially, the charge transfer between electrode and molecule is one of important reaction, and there are a lot of effort to improve the charge transfer reaction rate. The material design for the catalyst and complex chemical reaction have been suggested by theoretical and experimental studies [41, 42]. However, it is hard to describe the exact experimental charge transfer situation using first-principle approach [41]. The density functional theory usually fails to evaluate the experimental observed energy level difference of chemical system and charge transfer situation under the one-body description. Beyond the density functional theory calculation, the many-body and quantum chemistry calculation, such as GW and Moller-Plesser 2nd order perturbation calculations, are employed the describe the accurate chemistry system. On the other hand, enormous computational cost is required for these high accuracy calculation methods. As a temporary approach, the parametric Hubbard U potential is used to correct the quasiparticle level under the density functional theory scheme [18].

The wrong description of over-delocalized charge state is one of well-known problem in density functional theory calculation. This problem originates from the failure description of the on-site Coulomb interaction. Even though the distance between anion and cation is very far, for example, the non-zero charge transfer is depicted by the density functional theory. This failure is also reported in the solid system. For example, the band gap Mott insulator is induced by charge transition and density functional calculation fails to describe it. To correct the inaccurate on-site Coulomb interaction, parametric Hubbard U potential is employed, and the band gap of Mott insulator is successfully described as similar as experimental result. Therefore, the correction of on-site Coulomb interaction is required to describe the accurate charge transfer situation under the density functional theory scheme.

Among the various methodologies of molecular dynamics simulation, the ab initio molecular dynamics approach provides the time profiles of accurate chemical reaction including the change of chemical bond, charge transfer, and atomic position. This scheme based on the Born-Oppenheimer approximation that assumes adiabatic transition of electronic system. Under this approximation, on the other hand, the non-equilibrium dynamics of electron states is neglected and evaluates the inaccurate time scale of chemical reaction. In this study, time-dependent density functional theory calculation is used to describe the non-equilibrium dynamics of electron state under the Ehrenfest dynamics that treats the electronic and ionic motion simultaneously. In addition, the Hubbard U potential is implemented in the time dependent KS Hamiltonian to simulate the real time dynamics of charge transfer [7].

5.2. Inaccurate description of density functional theory in the long-range charge transfer situation.

To simulate the real time dynamics of charge transfer situation, the terephthalonitrile (TPN) potassium (K) system is employed as shown in Figure 5-1a. By the difference of electron negativity between K and TPN molecule, there can be charge transfer K atom to TPN molecule. The energy surface of TPN-K system with respect to distance between TPN and K atom is evaluated by Moller-Plesset 2nd order perturbation (MP2), which provides the chemically accurate description of exchange interaction between identical electron wavefunctions, as shown in Figure 5-1b. Interestingly, there is distinct kink point in the energy surface at 3.7 Å distance (Z) between K atom and TPN molecule. Based on the charge analysis for each fragment, it is revealed that there are single electron charge transfer between TPN molecule and K atom at short distance range (Z<3.7Å) and charge neutral state at long distance range (Z>3.7Å) under this chemical accurate calculation. Even though there is ionic bonding energy difference between restrict open shell (RO) and unrestricted (U) MP2 calculation, they show similar chemical trend which are the exothermic ionic bonding at short range and negligible bonding energy at long range.

This clear description of charge transfer fails with density functional theory calculation. With two types of local exchange-correlation functionals, the potential energy surfaces and transferred charges depending on the distance between TPN molecule and K atom as shown in Figure 5-1c and 5-1d. Unlike the MP2 calculation results, calculation results with PBE and LDA functionals show the continuous energy surface curves with non-zero binding energy at long distance (Z>5Å). The non-zero values of transferred charge at long distance (Z>5Å) are also described by the wrong description of on-site Coulomb interaction of density functional theory.

To remedy this problem, parametric Hubbard U potential is applied on the single K atom (U=4eV). The potential energy surface and transferred charge curves with additional Hubbard U potential are evaluated with respect to distance between TPN molecule and K atom shown in Figure 5-1e and 5-1f. The potential energy surface curve with Hubbard U potential indicates the two distinct curves which are deep potential well (red) and flat line (black). The transferred charge curve reveals that the deep potential energy well originates from the Coulomb potential between charge transferred ions and flat line describes negligible interaction between charge neutral KPN molecule and K atom. This result clearly shows that the additional Hubbard U potential remedies the wrong description of on-site Coulomb interaction in density functional theory calculation and improves the chemical accuracy similar as MP2 calculation.
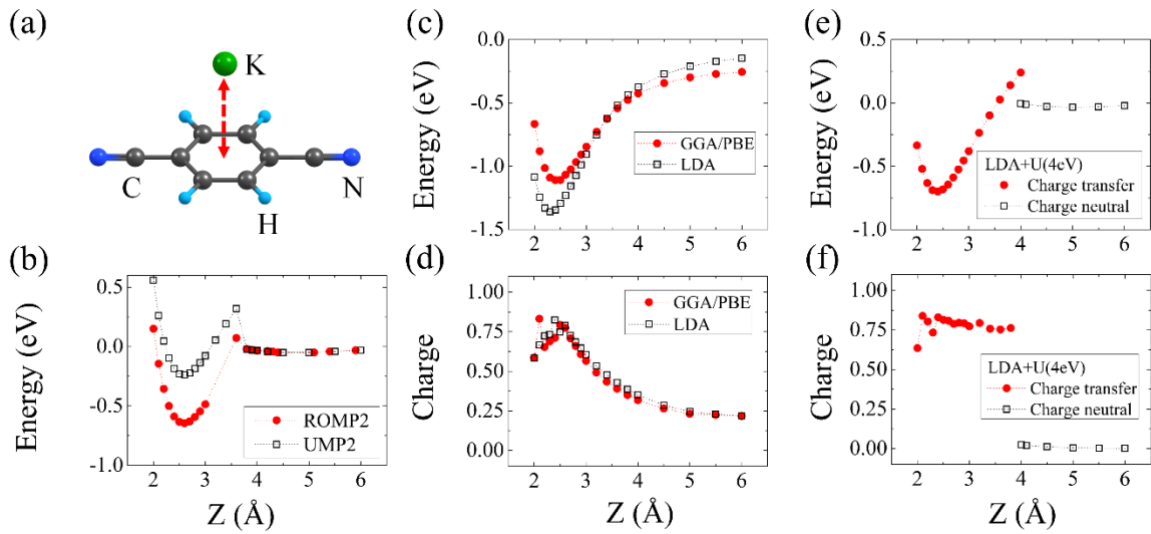
Figure 5-1. (a) schematic geometry of TPN-K. Potential energy curve with respect to distance between TPN molecule and K atom calculated by (b) MP2 correction method, density functional theory calculation with (c) and without (e) Hubbard U term on K atom (U=4). Transferred charge curve with respect to distance between TPN molecule and K atom evaluated by density functional theory calculation with (d) and without (f) Hubbard U term on K atom (U=4).

5.3. Real-time dynamics of charge transfer in TPN-K system

Under the accurate description of on-site Coulomb interaction by additional Hubbard U potential, the time-profile of charge transfer in TPN-K system is investigated using TDDFT. To simulate the charge transfer situation, charge neutral ground state of TPN molecule and K atom (Z=4.2Å) is used as an initial electronic structure and initial velocity of K atom toward the TPN atom is set as shown in Figure 5-2a. With three different initial kinetic energies of K atom, the time-profile of distance between TPN molecule and K atom are evaluated using TDDFT shown in Figure 5-2b. This result indicates that the distance between TPN molecule and K atom is linearly decreased by initial kinetic energy. The time-profiles of potential energy and transferred charge with initial Kinetic energy T_0=0.68eV are also calculated by TDDFT as shown in Figure 5-2c and 5-2d, respectively. The variation of total energy for electron system is negligible up to 40 fs. After the distance between TPN molecule and K atom is lower than 3.3Å at 40 fs, on the other hand, potential energy dramatically decreases and charge transfer is happened within 10 fs.

Unlike Born-Oppenheimer dynamics in ab initio molecular dynamics simulation, Ehrenfest dynamics in TDDFT calculation can describe the non-equilibrium dynamics of electronic structure. To investigate the non-equilibrium effect in the TPN-K system depending on the initial kinetic energy, the time-profiles of potential energy and transferred charge curves are compared with static ground state calculation results as shown in Figure 5-2e and 5-2f. Among three different initial kinetic energies, the potential energy curve with the highest initial kinetic energy shows the most deviation from the ground potential energy curve. In addition, the transferred charge curves also show the delated charge transfer position with higher initial kinetic energy. These results reveal that the non-equilibrium dynamics is significant to describe the molecular dynamics involving chemical reactions at high temperature.
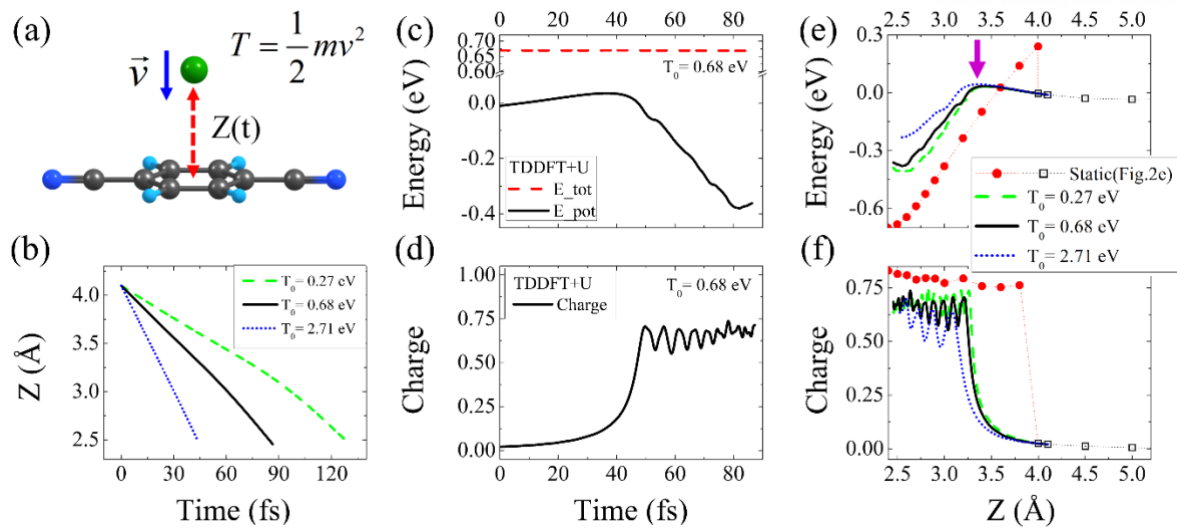
Figure 5-2. (a) Schematic initial condition of TPN-K. (b) Time profile of distance between TPN molecule and K atom depending on the initial kinetic energy of K atom. The time-profile of (c) potential energy and (d) charge transfer curves with 0.68 eV initial kinetic energy of K atom. (e) The potential energy and (c) charge transfer curves with respect to distance between TPN molecule and K atom calculated by static DFT and TDDFT.

5.4. The description of Anderson impurity model in the real-time dynamics

The dynamics situation between itinerant electron reservoir and localized impurity state have been studied using Anderson impurity model. This Hamiltonian with single defeat site can be written as

$$\hat{H} = \sum_{k,\sigma} \varepsilon_k \hat{a}_{k\sigma}^\dagger \hat{a}_{k\sigma} + \sum_\sigma \varepsilon_{d\sigma} \hat{c}_{d\sigma}^\dagger \hat{c}_{d\sigma} + \sum_{k,\sigma} V_{k,\sigma} \left(\hat{a}_{k\sigma}^\dagger \hat{c}_{d\sigma} + \hat{c}_{d\sigma}^\dagger \hat{a}_{k\sigma} \right) + U\hat{n}_{d\uparrow}\hat{n}_{d\downarrow} \quad (5\text{-}1)$$

The first and second terms of Eq. 5-1 indicate the itinerant states and defect site state, respectively. The third and last terms describes the hybridization interaction (V) between itinerant states and defect state and on-site Coulomb interaction (U) of defeat state, respectively. Depending on the interaction parameter V and U, the various correlated phenomena between itinerant states and defect site state can be described, such as Kondo effect. The non-equilibrium effect of this kind of correlated interaction can be evaluated by time propagation of this system. For example, the transition rate between itinerant and defect site states would be depending on the static U and V values and time dependent parameter as shown in Figure 5-3a.

Here, the real-time dynamics of Anderson impurity system is investigated in the material. The graphene with single Ca atom system is employed as shown in Figure 5-3b. The Ca atom locates far away from graphene hexagonal hollow site with distance Δ. For the initial condition, two electrons are artificially located in the Ca atom by static E-field. Before time propagation, the applied E-field is abruptly turned off and it induces the charge oscillation between graphene state and Ca atom. Based on the charge analysis, the time profile of charge state $Q(t)$ of Ca atom is calculated as shown in inset of Figure 5-3b. At the initial distance $\Delta=3\text{Å}$ and various Hubbard U value, the charge oscillation in the frequency domain $Q(\omega)$ is evaluated as shown in Figure 5-3c, while the charge oscillation of frequency domain is obtained by Fourier transform as follows $Q(\omega) = \text{Im}\left[\int_0^\infty Q(t) e^{i(\omega t+\phi)} dt \right]$.

Depending on the value of U on Ca atom, the peak position of oscillation frequency and amplitude are changed. It indicates that the Hubbard U potential is modulated the on-site Coulomb interaction (U) of the impurity Ca atom site and it reflects on the charge oscillation. Comparing with $\Delta=3.0\text{Å}$ and $\Delta=3.5\text{Å}$ cases, in addition, the peak position shift of the oscillation frequency is increased with longer distance as shown in Figure 5-3c and 5-3d. This variation reveals that the hybridization interaction (V) and the distance (Δ) between graphene and Ca atom are strongly correlated.
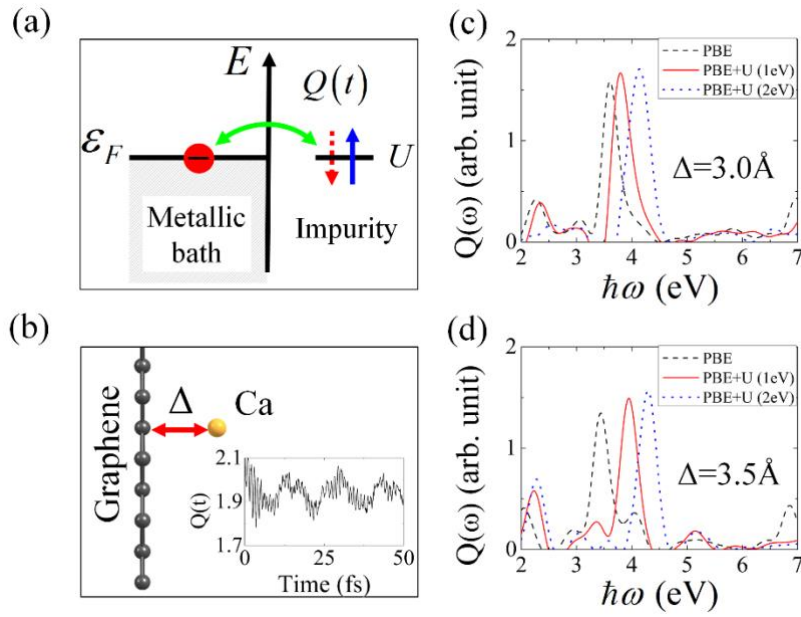
Figure 5-3. (a) The schematic state transition between itinerant state and impurity state. (b) Schematic geometry of graphene and Ca atom system with distance Δ. The charge oscillation in frequency domain with distance (c) Δ=3.0Å and (d) Δ=3.5Å between graphene and Ca atom. The inset of (b) indicates the time profile of charge oscillation.

5.4. Conclusion

In this study, the description of static and non-equilibrium charge transfer situation is investigated under the first principle approach. To remedy the electron over-delocalization problem of DFT which gives wrong description of charge transfer situation, the parametric Hubbard U potential is employed in the KS Hamiltonian. I found that this additional potential describes the accurate charge transfer situation as the quantum chemistry calculation MP2. Based on this calculation accuracy, the real-time dynamics of charge transfer is evaluated using TDDFT. In the TPN-K system, the ultrafast charge transfer (~10 fs) is evaluated regardless of the initial kinetic energy of system. In addition, it is found that the higher initial kinetic energy induces the non-equilibrium dynamics deviated from the ground state potential energy surface. Finally, the real-time dynamics of Anderson impurity system reveals the role of the parametric interaction and distance between itinerant states and impurity state. Based on these studies, the non-equilibrium dynamics of charge transfer can be accurately calculated in various chemical reactions.

VI. Summary

In this thesis, the various real-time dynamics calculations are introduced using TDDFT. In the TMDC material, the strong interaction between spin state and specific phonon mode is revealed by TDDFT calculation and phonon-induced spin magnetization is suggested. In the various topological material and insulator, it is found that the time-propagating Bloch states under the static E-field reveals the material Berry curvature and band topology. In last, the non-equilibrium dynamics of charge transfer is simulated with the correction of on-site Coulomb interaction by Hubbard U potential. These studies reveal the significance of real time dynamics and possibility of TDDFT calculation. Especially, the description of non-equilibrium dynamics is unique advantage of TDDFT. This methodology can be used to discover new fascinating physical phenomena beyond the DFT scheme.

Ⅶ. References

[1]   J. J. Sakurai and J. Napolitano, *Modern quantum mechanics*, 2nd ed. Boston: Addison-Wesley, 2011, pp. xviii, 550 p.

[2]   W. Kohn and L. J. Sham, "Self-Consistent Equations Including Exchange and Correlation Effects," *Phys. Rev.,* 140, no. 4A, pp. 1133-&, 1965.

[3]   G. F. Bertsch, J. I. Iwata, A. Rubio, and K. Yabana, "Real-space, real-time method for the dielectric function," *Phys. Rev. B,* 62, no. 12, pp. 7998-8002, 2000.

[4]   O. Sugino and Y. Miyamoto, "Density-functional approach to electron dynamics: Stable simulation under a self-consistent field," *Phys. Rev. B,* 59, no. 4, pp. 2579-2586, 1999.

[5]   D. Shin, H. Hübener, U. De Giovannini, H. Jin, A. Rubio, and N. Park, "Phonon-driven spin-Floquet magneto-valleytronics in MoS_2," *Nat. Commun.,* 9, p. 638, 2018.

[6]   D. Shin *et al.*, "Unraveling materials Berry curvature and Chern-Simons numbers from real-time evolution of Bloch states," arXiv:1809.07439, 2018.

[7]   D. Shin, G. Lee, Y. Miyamoto, and N. Park, "Real-Time Propagation via Time-Dependent Density Functional Theory Plus the Hubbard U Potential for Electron−Atom Coupled Dynamics Involving Charge Transfer," *J. Chem. Theory Comput.,* 12, pp. 201-208, 2016.

[8]   P. Hohenberg and W. Kohn, "Inhomogeneous Electron Gas," *Phys. Rev. B,* 136, no. 3B, pp. B864-&, 1964.

[9]   J. P. Perdew and A. Zunger, "Self-Interaction Correction to Density-Functional Approximations for Many-Electron Systems," *Phys. Rev. B,* 23, no. 10, p. 5048, 1981.

[10]   J. P. Perdew, K. Burke, and M. Ernzerhof, "Generalized gradient approximation made simple," *Phys. Rev. Lett.,* 77, no. 18, pp. 3865-3868, 1996.

[11]   L. Hedin, "New Method for Calculating 1-Particle Greens Function with Application to Electron-Gas Problem," *Phys. Rev.,* 139, p. A796, 1965.

[12]   F. Lechermann, L. Boehnke, D. Grieger, and C. Piefke, "Electron correlation and magnetism at the LaAlO3/SrTiO3 interface: A DFT plus DMFT investigation," *Phys. Rev. B,* 90, no. 8, p. 085125, 2014.

[13]   G. Kresse and J. Furthmuller, "Efficient iterative schemes for ab initio total-energy calculations using a plane-wave basis set," *Phys. Rev. B,* 54, no. 16, pp. 11169-11186, 1996.

[14]   P. Giannozzi *et al.*, "QUANTUM ESPRESSO: a modular and open-source software project for quantum simulations of materials," *J. Phys-Condens. Mat.,* 21, no. 39, p. 395502, 2009.

[15]   X. Andrade *et al.*, "Real-space grids and the Octopus code as tools for the development of new simulation approaches for electronic systems," *Phys. Chem. Chem. Phys.,* 17, no. 47, p. 31371, 2015.

[16]   D. Vanderbilt, "Soft Self-Consistent Pseudopotentials in a Generalized Eigenvalue Formalism," *Physical Review B,* 41, no. 11, pp. 7892-7895, 1990.

[17]   A. I. Liechtenstein, V. I. Anisimov, and J. Zaanen, "Density-Functional Theory and Strong-Interactions - Orbital Ordering in Mott-Hubbard Insulators," *Phys. Rev. B,* 52, no. 8, pp. R5467-R5470, 1995.

[18]   H. J. Kulik and N. Marzari, "Accurate potential energy surfaces with a DFT plus U(R) approach," *J. Chem. Phys.,* 135, no. 19, p. 194105, 2011.

[19]   N. Tancogne-Dejean, M. A. Sentef, and A. Rubio, "Ultrafast Modification of Hubbard U in a Strongly Correlated Material: Ab initio High-Harmonic Generation in NiO," *Phys. Rev. Lett.,* 121, no. 9, p. 097402 2018.

[20]   E. Runge and E. K. U. Gross, "Density-Functional Theory for Time-Dependent Systems," *Phys. Rev. Lett.,* 52, no. 12, p. 997, 1984.

[21]   A. Castro *et al.*, "octopus: a tool for the application of time-dependent density functional theory," *Phys. Status. Solidi. B,* 243, no. 11, pp. 2465-2488, 2006.

[22]   R. M. Martin, *Electronic structure : basic theory and practical methods*, 1st pbk. ed. Cambridge, UK ; New York: Cambridge University Press, 2008, pp. xxii, 624 p.

[23]   K. F. Mak, K. L. He, J. Shan, and T. F. Heinz, "Control of valley polarization in monolayer MoS_2 by optical helicity," *Nat. Nanotechnol.,* 7, no. 8, p. 494, 2012.

[24]   H. L. Zeng, J. F. Dai, W. Yao, D. Xiao, and X. D. Cui, "Valley polarization in MoS_2 monolayers by optical pumping," *Nat. Nanotechnol.,* 7, no. 8, p. 490, 2012.

[25]   D. Xiao, G. B. Liu, W. X. Feng, X. D. Xu, and W. Yao, "Coupled Spin and Valley Physics in Monolayers of MoS_2 and Other Group-VI Dichalcogenides," *Phys. Rev. Lett.,* 108, no. 19, p. 196802, 2012.

[26]   Y. T. Wang *et al.*, "Ultrafast Multi-Level Logic Gates with Spin-Valley Coupled Polarization Anisotropy in Monolayer MoS_2," *Sci. Rep.,* 5, p. 8289, 2015.

[27]   M. V. Berry, "Quantal Phase-Factors Accompanying Adiabatic Changes," *Proc. R. Soc. Lon. Ser-A,* 392, no. 1802, pp. 45-57, 1984.

[28]   D. Xiao, M. C. Chang, and Q. Niu, "Berry phase effects on electronic properties," *Rev. Mod. Phys.,* 82, no. 3, pp. 1959-2007, 2010.

[29]   D. Xiao, W. Yao, and Q. Niu, "Valley-contrasting physics in graphene: Magnetic moment and topological transport," *Phys. Rev. Lett.,* 99, no. 23, p. 236809, 2007.

[30]   D. J. Thouless, M. Kohmoto, M. P. Nightingale, and M. denNijs, "Quantized Hall Conductance in a Two-Dimensional Periodic Potential," *Phys. Rev. Lett.,* 49, no. 6, pp. 405-408, 1982.

[31]   F. D. M. Haldane, "Model for a Quantum Hall-Effect without Landau-Levels - Condensed-Matter Realization of the Parity Anomaly," *Phys. Rev. Lett.,* 61, no. 18, pp. 2015-2018, 1988.

[32]   C. L. Kane and E. J. Mele, "Quantum spin Hall effect in graphene," *Phys. Rev. Lett.,* 95, no. 22, p. 226801, 2005.

[33]   B. A. Bernevig, T. L. Hughes, and S. C. Zhang, "Quantum spin Hall effect and topological phase transition in HgTe quantum wells," *Science,* 314, no. 5806, pp. 1757-1761, 2006.

[34]   C. L. Kane and E. J. Mele, "Z(2) topological order and the quantum spin Hall effect," *Phys. Rev. Lett.,* 95, no. 14, p. 146802, 2005.

[35]   N. H. Lindner, G. Refael, and V. Galitski, "Floquet topological insulator in semiconductor quantum wells," *Nat. Phys.,* 7, no. 6, p. 490, 2011.

[36]   M. BenDahan, E. Peik, J. Reichel, Y. Castin, and C. Salomon, "Bloch oscillations of atoms in an optical potential," *Phys. Rev. Lett.,* 76, no. 24, pp. 4508-4511, 1996.

[37]   S. C. Wu, G. C. Shan, and B. H. Yan, "Prediction of Near-Room-Temperature Quantum Anomalous Hall Effect on Honeycomb Materials," *Phys. Rev. Lett.,* 113, no. 25, p. 256401, 2014.

[38]   K. H. Jin and S. H. Jhi, "Quantum anomalous Hall and quantum spin-Hall phases in flattened Bi and Sb bilayers," *Sci. Rep.,* 5, p. 8426 2015.

[39]   O. F. Dayi and E. Yunt, "Relation between the spin Hall conductivity and the spin Chern number for Dirac-like systems," *Int. J. Geom. Methods M.,* 13, no. 1, p. 1550136, 2016.

[40]   T. Oka and H. Aoki, "Photovoltaic Hall effect in graphene," *Phys. Rev. B,* 79, no. 8, p. 081406(R), 2009.

[41]   D. Shin, H. Jung, S. S. Han, C. H. Choi, H. Lee, and N. Park, "Microscopic nature of mobile fluoride anions on sp(2) carbon surfaces," *Chem. Phys. Lett.,* 570, pp. 85-89, 2013.

[42]   D. Shin, S. Sinthika, M. Choi, R. Thapa, and N. Park, "Ab Initio Study of Thin Oxide−Metal Overlayers as an Inverse Catalytic System for Dioxygen Reduction and Enhanced CO Tolerance," *ACS Catalysis,* 4, p. 4074, 2014.

VIII. Acknowledgements